Characterization and Readout of 3D Silicon Microdosimeters

by

Øyvind Lye

THESIS
for the degree of
MASTER OF SCIENCE IN PHYSICS

(Specialisation in Microelectronics)

Department of Physics and Technology
University of Bergen

September 2016

Contents

Chapter 1: Introduction

1.1 Background and Motivation

In 2013 the Norwegian government started a project to build centers for cancer treatment using particle radiotherapy. The main reason for this is that radiotherapy using heavy charged particles does less damage to healthy tissue than the more conventional radiotherapy using photons that Norway has today. Many photon radiotherapy patients develops cancer again a few decades after the original treatment as a result of the treatment radiation, which makes photon radiotherapy little suited for treating cancer in children. Every year 1000 to 1500 Norwegians will experience fewer side effects by being treated with protons instead of photons [Lynnebakken, 2012]. When treating cancer with heavy charged particles it is critical to be able to deposit the energy of the radiation at the correct position inside the patient, both to kill the tumor and to avoid unnecessary damage to healthy tissue around the tumor. More on this in section 2.2.1.

To be able to assure the quality of the treatment system, the hospitals need to be able to predict how the energy from a beam of heavy charged particles will be absorbed in the body. The uncertainties because of the lack of knowledge on this causes an increased risk of side effects for proton therapy patients. To bolster the research on the effects of radiation on humans, SINTEF is developing a silicon based radiation detector, named 3DMiMic, which mimics the response of biological tissue to ionizing radiation on a cellular and sub-cellular level. By measuring how the energy is distributed in the detector, researchers will will learn more about how a patient will react to the same radiation beam. [SINTEF, 2015]

1.2 Goal of the Thesis

1.3 Structure of the Thesis

Chapter 1: Introducton
Introduces the thesis, including background, motivation and goals.

Chapter 2: Radiation and Radiotherapy
Important background theory for full understanding of the thesis. Includes theory of

ionizing radiation, biological effects of radiation, and radiotherapy.

Chapter 3: Testing and Characterization of the 3DMiMic Detector Includes important background theory about radiation detectors, an introduction to the 3DMiMic detectors, and measurement results from the detectors.

Chapter 4: Choice of Readout Electronics for the 3DMiMic Detector Background theory on detector readout, and short introductions to the main readout electronics that was considered for this project.

Chapter 5: Characterization of IDE1180 Measurement setups, results, and conclusions from the characterization of the IDE1180 pre-amplifier shaper from IDEAS.

Appendix A: 3DMiMic Layouts Figures and explanations on the different 3DMiMic layouts and wafers.

Appendix B: Detector Interface PCB Description of the interface PCB that was made for the 3DMiMic detectors. Includes pictures of how the detectors should be wire-bonded to the PCB.

Appendix C: List of Readout Electronics Table including all readout electronics that was considered for the project with relevant specifications.

1.3.1 Note on Citations

Citations in this thesis generally follows the guidelines recommended for Wikipedia authors. A citation placed after the last punctuation in a paragraph supports multiple claims through the paragraph, while a citation placed before a punctuation only supports one or a few claims just before the citation. In this thesis, citations at the end of a paragraph is much used in the theory sections, where they refer to sources with more detailed information for the interested reader.

1.4 Scientific Environment

This master project is supervised by Professor Kjetil Ullaland in the electronics and measurement science research group at the Department of Physics and Technology (IFT) at the University of Bergen (UiB). The 3DMiMic project is a part of the subatomic physics research group at IFT and this master project was assigned by Professor Dieter Röhrich of this group. The Ph.D. dissertation of Röhrich's student Andreas Tefre

Samnøy shares many of this master projects objectives. Post doctor Kristian Smeland Ytre-Haugen at IFT leads an ongoing project that looks into microdosimetry and relative biological effectiveness of proton and heavy ion therapy.

SINTEF's department of Microsystems and Nanotechnology produces the 3DMiMic pixel detector that this project is based on. The University of Oslo (UiO) and the University of Wollongong (UOW) is also involved in the 3DMiMic project.

Chapter 2: Radiation and Radiotherapy

2.1 Radiation

Radiation is defined as the emission and propagation of energy through space or a material medium. Previously radiation was split into groups depending on if it was transferred through particles or waves. This was changed after 1924 when Louis de Broglie claimed that all matter has a wave-like nature. Now, *particle radiation* refers to energy propagated by particles with a definite rest mass and within limits at any instant have a definite momentum and defined position. A particle beam is a group of particles that move in the same direction, similar to a light beam. Examples of these particles are electrons, neutrons, protons, and heavy ions. *Electromagnetic radiation* is energy propagated by the massless photons in phenomena such as light waves, radio waves, microwaves, X-rays, and gamma (γ) rays. Electromagnetic waves propagate at the speed of light and are represented by the spatial intensity variations of an electric field and a magnetic field. [Khan and Gibbons, 2014, chap. 1]

Ionizing radiation carries enough energy to break molecular bonds by *ionizing* atoms it passes, meaning that the atom acquires a positive or negative charge. If the radiation strips an electron from the atom, it becomes a positive ion. If a stripped electron later combines with a neutral atom, it becomes a positive ion. Charged particles with enough kinetic energy is called *directly ionizing radiation* because they can ionize atoms through collisions. Uncharged particles are known as *indirectly ionizing radiation* as they *excite* atoms, raising electrons to higher energy levels. An excited atom can later emit directly ionizing radiation through an electron. [Khan and Gibbons, 2014, chap. 5] See section 2.1.1 for more on this.

2.1.1 Interactions of Radiation with Matter

Interactions of charged particles with matter

Charged particles, for example protons, primarily react by ionization and excitation. Electrons also commonly react through bremsstrahlung (deceleration radiation), where the particle is decelerated and emits the lost kinetic energy as a photon. When charged particles travel through a medium, they interact with atomic electrons and nuclei through the Coulomb force. These interactions can be inelastic collisions with atomic electrons, or elastic scattering without energy loss. In the inelastic collisions, the particle looses part of its kinetic energy to produce ionizations and excitations of atoms. This results in energy being absorbed in the medium as the particle is decelerated. [Khan and Gibbons, 2014, chap. 5 & 27]

Stopping power is the average rate of energy loss of a particle per unit path length ($-dE/dx$) in a medium. The Linear Energy Transfer (LET) of a particle is the energy locally deposited per length and is usually expressed in MeV/cm or $keV/\mu m$. The LET will always be equal to or smaller than the stopping power. These parameters are used to describe energy deposition in matter and the biological effect of radiation (see section 2.1.2). The LET of a heavy charged particle (a particle of equal or greater mass than a proton) travelling through matter is inversely proportional to the square of its velocity. This means that as the particle looses energy and slows down, the rate of energy loss will increase and the particle slows down at a faster rate. The rate of energy loss (and energy deposition in the medium) becomes maximum as the particle velocity approaches zero. This leads to the particle stopping relatively quickly after travelling a certain distance and makes it possible to define a range for a certain type of particle with a defined energy in a type of matter. The intensity of a particle beam plotted versus depth in tissue can be seen in figure 2.1 where the sudden drop in the proton plots is defined as the particle's range for that energy. [Khan and Gibbons, 2014, chap. 27]

Interactions of photons with matter

The five dominating processes for photon interactions with matter are Rayleigh scattering, the photoelectric effect, the Compton effect, pair production, and photodisintegration. Rayleigh scattering happens when a low energy photon collides with an electron and is scattered to a different angle. This does not deposit any energy in the medium, but the photon is scattered away from its original path. The photoelectric effect is a phenomenon where all the energy of a photon is absorbed in an atom. This leads to one of the orbital electrons being emitted, and the shell vacancy will lead to emission of X-rays as a higher energy electron fills the vacancy. Occasionally, these X-rays will also cause more electrons to be emitted. The Compton effect is when a photon collides with an atomic bound electron, scattering the photon and transferring some of its energy to the electron. This is given to the electron as kinetic energy. Pair production can happen with photons of energy greater than 1.022 MeV, where a photon travelling near an atomic nucleus gives all its energy to produce an electron and a

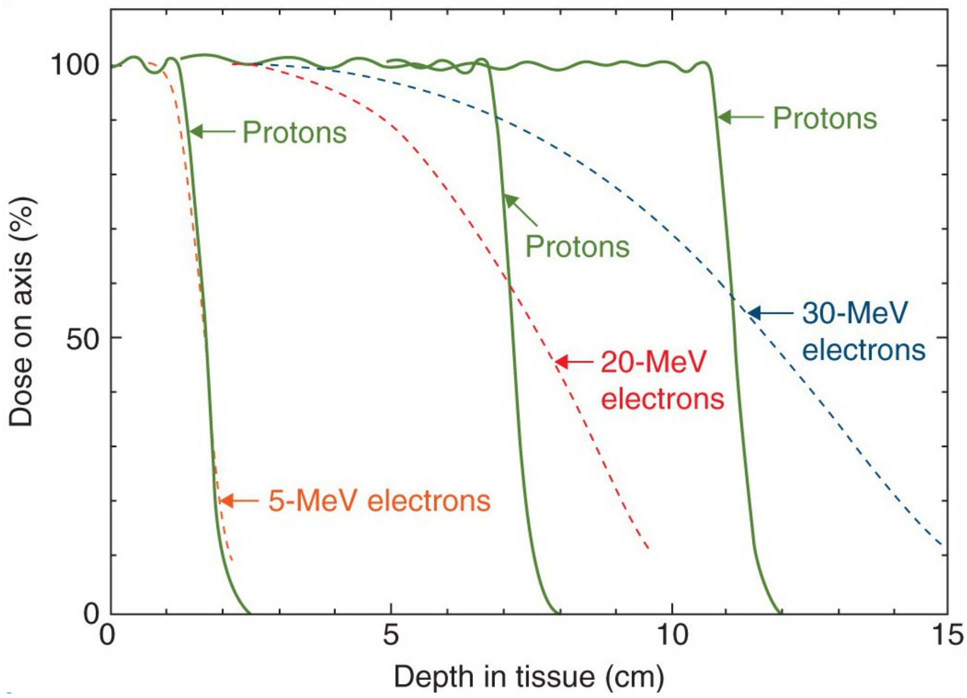

Figure 2.1: Comparison of depth dose distribution for protons and electrons of different energies. [Khan and Gibbons, 2014, fig. 5.15]

positron. The positron will later find an atomic electron and they will annihilate each other by producing two photons of 0.511 MeV each. A high energy photon can cause photodisintegration by reacting with an atomic nucleus, leading to a nuclear reaction. [Khan and Gibbons, 2014, chap. 2 & 5]

Due to all the above processes, a photon travelling through matter will at each instant in time have a certain chance of being absorbed or scattered by the medium. Because of this, the intensity of a photon beam will start to go down instantly when it leaves vacuum, but will take a very long time to be reduced to zero, see figure 2.2. It is therefore very difficult to simply define the range of a photon beam, as can be done with a beam of heavy charged particles. The reduction in the number of photons is proportional to the number of incident photons through the *attenuation coefficient*. [Khan and Gibbons, 2014, chap. 5]

2.1.2 Biological Effects of Radiation

As discussed in the previous sections, radiation travelling through matter deposits energy in the medium. Examining the effects of this in biological tissue is an extremely complex field. Non-ionizing radiation can heat the matter it passes through. Ionizing radiation is much more dangerous as it breaks molecular bonds, causing molecules to

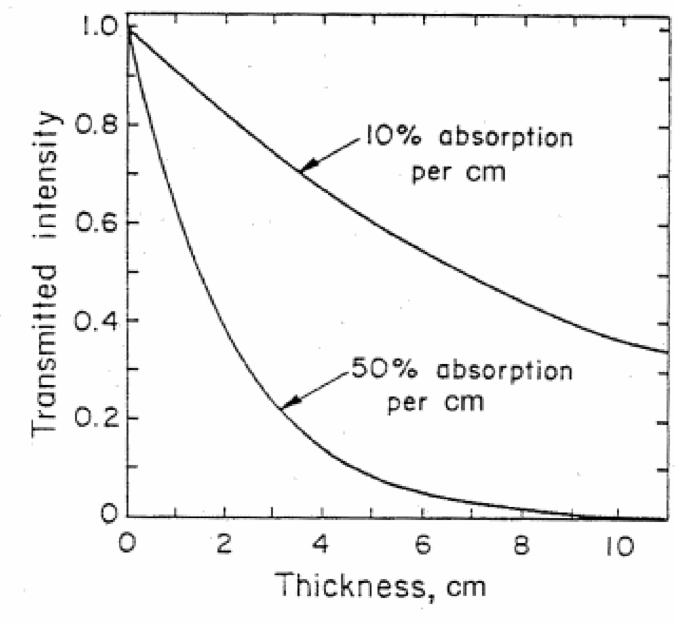

Figure 2.2: Photon intensity through an absorber as a function of thickness [ASU, 2000]

fall apart. This can cause massive damage to tissue cells, change the genetic material (DNA), and destroy the components that produce red blood cells. [Young et al., 2007, chap. 43]

When a cell has been damaged by radiation, there are three possible effects: The cell dies, the cell is repaired correctly, or the cell is repaired incorrectly. The human body has very effective repair mechanisms which constantly repair cellular damage, including damage to DNA. Occasionally, these repair mechanisms will perform their function incorrectly, which can result in cells that cannot perform their normal function, or cells that damage other cells. Some of these cells are unable to reproduce themselves, while others reproduced at an uncontrolled rate, which can be the cause of cancers.[JLab]

To be able to describe the quantity of ionizing radiation for all energies, materials, and types of radiation, it is common to use the quantity *absorbed dose*, or simply *dose*, which can be used as a measure of the biologically significant effects that ionizing radiation produces. It is defined as the radiation energy delivered to tissue per unit mass. The SI unit for dose is gray (Gy), where $1Gy = 1J/kg$. The quantity *dose equivalent* has been defined because the biological effects of radiation depend on the type of radiation in addition to the dose. Dose equivalent is the dose multiplied by a quality factor for the type of radiation, in units of sievert (Sv). $1Sv = 1J/kg$. Additionally, the sensitivity to radiation-induced effects will vary for different types of tissue, leading to the definition of *effective dose equivalent*, defined as "the sum of the weighted dose equivalents for irradiated tissues or organs". [Khan and Gibbons, 2014, chap. 8 & 16]

2.2 Radiation Therapy

Radiation therapy, also known as radiotherapy, is therapy using the biological effects of ionizing radiation to kill or control cancer cells. One of the main principles behind radiotherapy's effectiveness in treating cancer is that radiation causes much more damage to rapidly dividing cells, and tumor cells divide extremely rapidly [Serway and Jewett, 2014, chap. 45]. Roughly half of all cancer patients receive radiotherapy as a part of their treatment. The radiation can originate from a machine outside the body (external beam radiation therapy), or from a radioactive source being placed into the body (internal radiation therapy). Traditional external beam radiation therapy is delivered using photon beams (photon therapy), but treatment with beams of heavy charged particles (particle therapy), like protons (proton therapy) or carbon ions, are becoming more common. Electron beam therapy is also used, mainly to treat cancer close to the surface of the body. [NIH, 2010]

The radiation will also damage healthy tissue, but a lot of work is put into reducing this as much as possible. Planning and simulations are done to increase the certainty of avoiding complications. Detailed imaging scans are done to get a 3D map of the patient's tumor and surrounding areas. The basis for these maps are usually Computed Tomography (CT) scans, but can also be combined with Magnetic Resonance Imaging (MRI), Positron Emission Tomography (PET), X-ray images, or ultrasound scans [NIH, 2010]. One of the main reasons for CT's importance for photon therapy is that as it is based on photon beams, a CT scan also yields the body's tissue-density information and photon attenuation coefficient, which is needed for photon therapy planning. [Khan and Gibbons, 2014, chap. 12]

The particle beams of external beam radiation therapy are of high energy and needs to be produced in or near the treatment machine. For photon therapy, it is most common to accelerate photons using a linear accelerator (linac), which is small enough to fit inside the same room as the patient table [NIH, 2010]. For particle therapy a bigger and more expensive accelerator is needed to accelerate the particles to high enough energies. For proton therapy a cyclotron or a synchrotron is used. [Khan and Gibbons, 2014, chap. 27]

A patient treatment dose is usually delivered once per day every workday for 4-6 weeks. One delivery is called a fraction. Fractionation is done for multiple reasons: One is to allow healthy tissue time to repair the damage from radiation. Another is to increase the chance of hitting the cancer cells at a time when they are vulnerable. Fractionation also helps to minimize the effects of random variations in the patient's position and internal geometry. [Board of the Faculty of Clinical Radiology, 2006] [Hysing, 2015]

As already mentioned, radiation therapy also damages healthy tissue, which can produce both acute (early) and chronic (late) side effects. Acute side effects occur before the treatment ends, and is usually temporary. Examples include skin irritation, hair loss, fatigue and nausea. Chronic side effects develop months to decades after treatment is complete. Examples are skin damage, memory loss, infertility and secondary cancer. Secondary cancer is the development of a new cancer in a person that has previously had cancer. As this takes a long time to develop, it might not be a very large problem for older patients, but it is critical to avoid secondary cancer when treating cancer in children and adolescents. [NIH, 2010]

When plotting the absorbed dose in water (or tissue), the differences between photon beams and heavy charged particle beams become even more apparent than when plotting the intensities (section 2.1.1). Figure 2.3 shows the relative dose deposited in water for a proton and a photon beam. The photon beam's maximum is very close to the surface, and the photons will damage tissue far into the body. Also, if the tumor is deep into the body, and the beam only comes from one direction, the photons will have to do a lot of damage to the skin to be able to do enough damage to the tumor. Protons (and other heavy charged particles) on the other hand have their maximum deeper into the material, in what is called the *Bragg peak*. Protons deposit less energy before the maximum, and close to no damage behind the maximum.

2.2.1 Proton Therapy

Proton therapy is radiation therapy using high energy proton beams. The main principle behind the use of proton therapy is to exploit the Bragg peak to deposit a high dose to a tumor, with low dose delivered in front of it, and close to no dose behind. The Bragg peak is very narrow and is not able to cover most tumors, which has lead to the use of superposition of multiple beams of different energies. This superposition is called a Spread-Out Bragg Peak (SOBP), see figure 2.4. A SOBP has a lot higher dose deposited in front of the tumor than a single proton beam, but it is still lower than that of a photon beam. The dose behind the tumor is still low. [Khan and Gibbons, 2014,

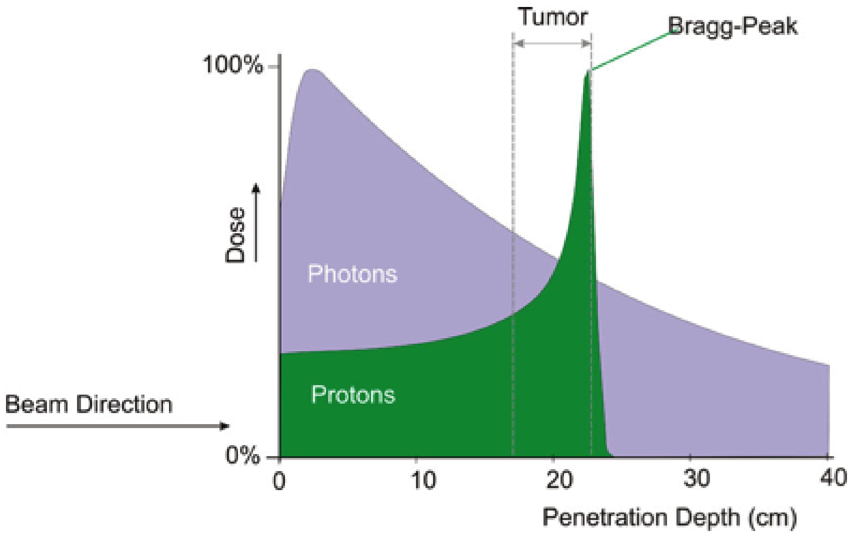

Figure 2.3: Percentage depth dose for a photon beam and a proton beam in tissue. [P-Cure]

chap. 27]

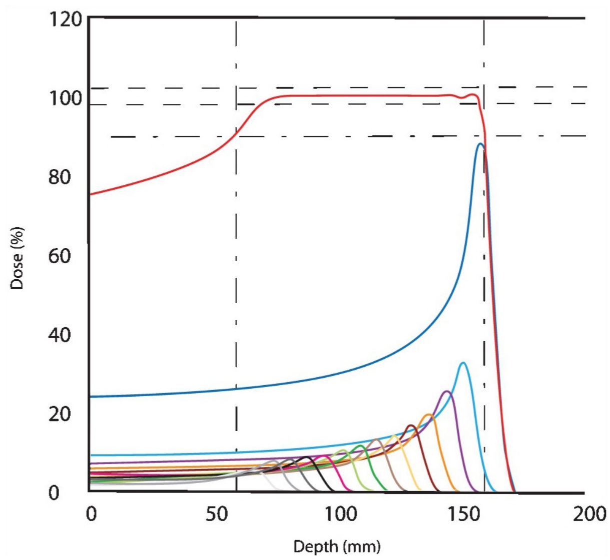

Figure 2.4: SOBP depth dose distribution [Khan and Gibbons, 2014, fig. 27.10]

The shape of the SOBP makes it possible to treat tumors with a lot less dose to the surrounding tissue than with photon therapy, which has two main benefits. One is the ability to treat tumors in close proximity to critical organs without damaging said organ. The other is to avoid the chronic side effects mentioned in section 2.2, which is very important when treating children with cancer [Khan and Gibbons, 2014, chap. 27]. Figure 2.5 compares photon (A) and proton (B) beams, where red is high dose, blue is low dose, and gray is negligible dose.

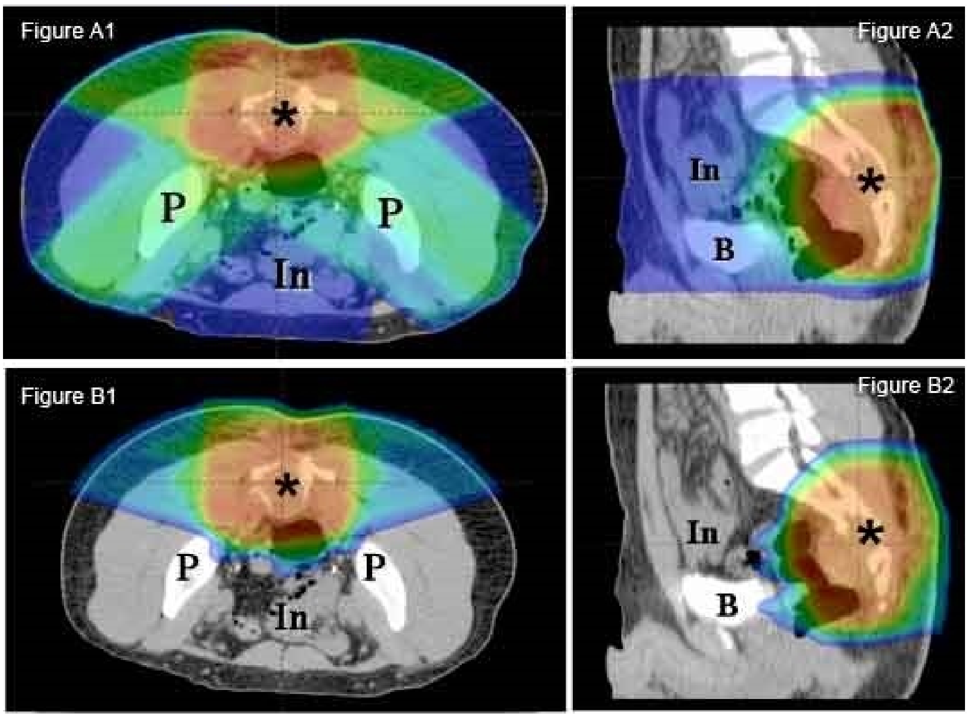

Figure 2.5: Photon (A1 & A2) and proton (B1 & B2) beam dose distributions. [P-Cure]

The geometrical accuracy in proton therapy is a lot more critical than in photon therapy. While a geometrical error between planning and delivery in photon therapy will give a smaller under-dosage to the tumor and over-dosage to surrounding tissue, similar errors in proton therapy could cause part of the tumor receiving no dose at all and healthy tissue receiving full dose, see figure 2.6. Geometrical uncertainties can come from setup and anatomical variations, biological considerations, organ motion, and dose calculation approximations. [Paganetti, 2012]

As mentioned in section 2.2, photon CT yields the patient's photon attenuation coefficient that is needed for photon therapy, but for proton therapy the stopping power is needed to greatly reduce range errors. Therefore proton CT imaging techniques are being developed, based on the same principles as conventional CT, but using low-intensity proton beams instead of photon beams. [Freeman, 2013]

Proton therapy can theoretically be delivered in fewer fractions than photon therapy due to lower dose to surrounding tissue, but this is more risky in case the target is missed.

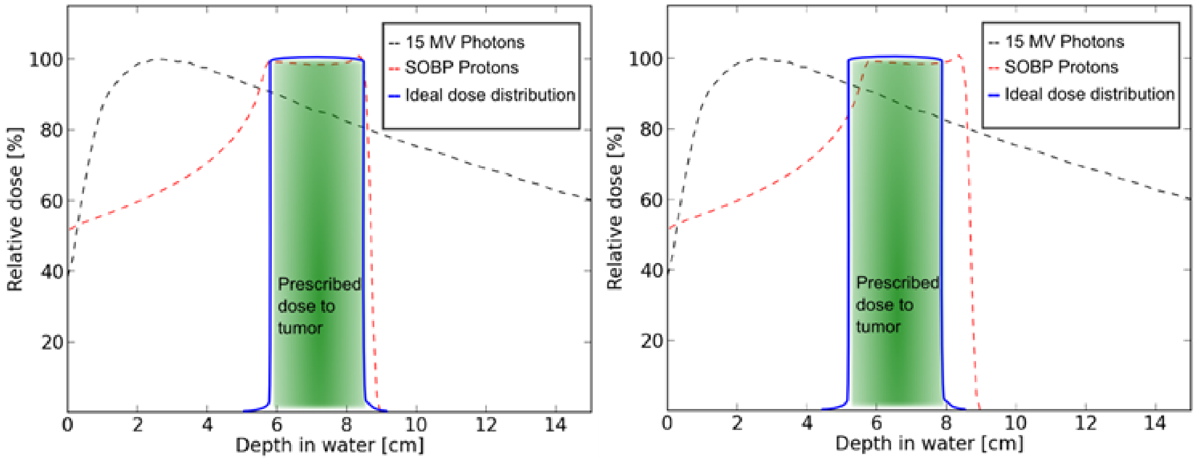

Figure 2.6: Comparison of dose distribution with correct (left) and incorrect (right) range assumptions. [Ytre-Hauge, 2015]

2.2.2 Carbon Therapy

Carbons have also been used clinically for radiotherapy since 1994 in Japan, and 2002 in Germany. Data from these centers suggest that carbon therapy is superior to proton therapy for certain types of cancer. By comparing depth dose distributions, figure 2.7, the carbon ion shows a sharper Bragg peak, but the dose is not reduced to zero after the Bragg peak. This suggests that carbon therapy might be worse than proton therapy when there is a critical organ just behind the tumor. For certain cancer types can however benefit from the sharper Bragg peak, lower entrance dose, and lower lateral spread of dose 2.7. As carbons are heavier, they also require more complex and expensive accelerators than protons. [Ytre-Hauge, 2015]

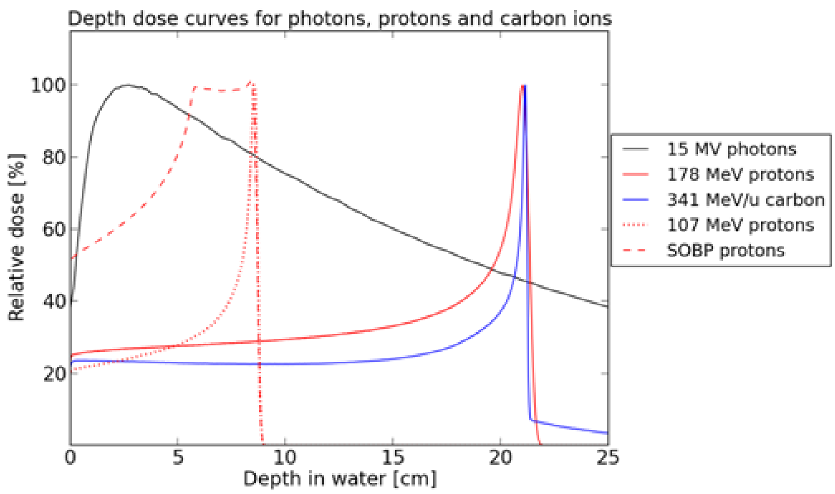

Figure 2.7: Comparison of photon, proton, and carbon depth dose distributions. [Ytre-Hauge, 2015]

Chapter 3: Testing and Characterization of the 3DMiMic Detector

3.1 Radiation Detectors

A radiation detector records interactions between incoming radiation and the detector. These interactions could be electrical, chemical, light- or heat-based. Detectors can be based on many different materials, including gas chambers, semiconductors, crystals, and liquid. In a simple radiation detector a single particle interacts with the detector, resulting in an electric charge appearing inside the detector. This charge is typically collected by setting up an electric field inside the detector, which causes positive and negative charge to flow in opposite directions, forming an electric signal. This signal could be measured as a current (current mode), voltage (mean square voltage mode), or a charge (pulse mode). [Knoll, 2010, chap. 4]

Pulse mode is the most common readout mode because the measurement records each individual quantum of radiation. Pulse mode is therefore required when attempting to measure the energy of individual radiation events. The charge generated in the detector is usually integrated over a certain period of time. Pulse mode however does not work well at very high event rates as the time between events becomes too short to analyse the data. Current mode measures the average current over many events, therefore loosing the amplitude and timing information of individual events, but allowing for measurement with high event rates. Mean square voltage mode works much like current mode, but the output signal will be more dependent on the charge per event, making this mode more useful for mixed radiation environments. [Knoll, 2010, chap. 4]

3.1.1 Semiconductor Detectors

Semiconductor diode detectors, also called simply semiconductor detectors or solid-state detectors, are radiation detectors employing semiconductor diodes as the basic detection medium. Silicon is the most common material used, but germanium detectors are superior for gamma-ray measurements. Semiconductor detectors offer energy resolutions that are superior to other radiation detectors in addition to small size and fast timing characteristics. A big drawback is that they are degraded by radiation-induced damage during normal use. [Knoll, 2010, chap. 11]

Charged particles passing through a semiconductor detector create electron-hole pairs along the particles path. By setting up an electric potential across the diode, there will be an electric field present that will cause the holes to drift in the same direction as the electric field vector, and the electrons in the opposite direction. By monitoring one of the diodes sides, a pulse is measured as the charge from either the holes or the electrons (depending on which side is measured) is collected.

A semiconductor detector, like other diodes, can be forward biased (positive potential on p-side) or reverse biased (positive potential on n-side). It is possible to operate a semiconductor detector without external bias, but it will perform poorly as the electric field across the junction will be too weak to read out the charge carriers before many are lost. Applying forward bias to the detector reduces the electric field even further, while reverse bias increases it. Another important factor is that reverse bias increases the depletion region, which is also the active volume of the detector. [Knoll, 2010, chap. 11]

3.2 Semiconductor Characterization

3.2.1 Capacitance-Voltage Measurements

Capacitance-Voltage (C-V) profiling is a semiconductor characterisation technique that is much used to find doping- and defect densities in semiconductor junctions. The technique relies on the fact that the width of a reverse biased depletion region depends on the applied voltage. The small signal capacitance is dependent on both the doping density and width of the depletion region. C-V profiles are made by measuring the capacitance while sweeping over a voltage range. The doping density is found from the slope of a C-V curve or a $1/C^2$-V curve. [Schroder, 2005, chap. 2]

There are multiple ways to measure capacitance. A simple method is to supply a known current, and measure how fast the voltage across the capacitor rises. This method assumes an ideal capacitor, and is therefore inaccurate for a real capacitor. A more accurate method is to supply an AC signal to the Device Under Test (DUT) and measure the AC current and voltage. A high frequency signal ($\sim$10 MHz) will be better for measuring dynamic performance, while a low frequency signal ($\sim$10 kHz) is better to find quasistatic characteristics. The capacitance is calculated from the fre-

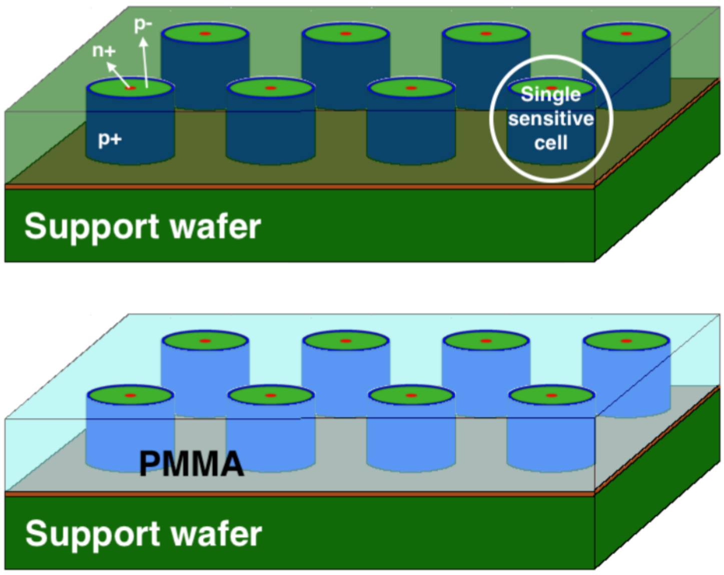

Figure 3.1: Presentation sketches of the 3DMiMic detector, shown without and with PMMA. [Povoli et al., 2015]

quency, current, and voltage.

3.2.2 Current-Voltage Measurements

Current-Voltage (I-V) characterization is observation of the current through a device when sweeping over the voltage across it. This can be used to find basic electrical parameters for the device. This includes leakage current, resistance, cut-in voltage, breakdown voltage, saturation voltage, and hysteresis.

3.3 3DMiMic

Si-3DMiMic, or simply 3DMiMic, is a silicon-based 3D mini and micro-dosimeter being developed by SINTEF MiNaLab in Oslo, but was invented and ordered by Professor Anatoly Rozenfeld from the Centre for Medical Radiation Physics at the University of Wollongong. The detector is made to mimic the response of biological tissues to ionizing radiation on a cellular and sub-cellular level, and consists of an array of more than a thousand cylindrical p-i-n diodes (see figure 3.1). Each diode, or cell, is made of a thin n+ core cylinder, a circular p+ trench some micrometers out, and in some cases a n+ guard ring further away from the core (see figure 3.2). There are multiple versions of the detectors, with differences including presence of n+ guard ring, size of cell, and structure. The silicon between the different cells should be etched away and replaced with tissue equivalent polymethyl methacrylate (PMMA), but this has

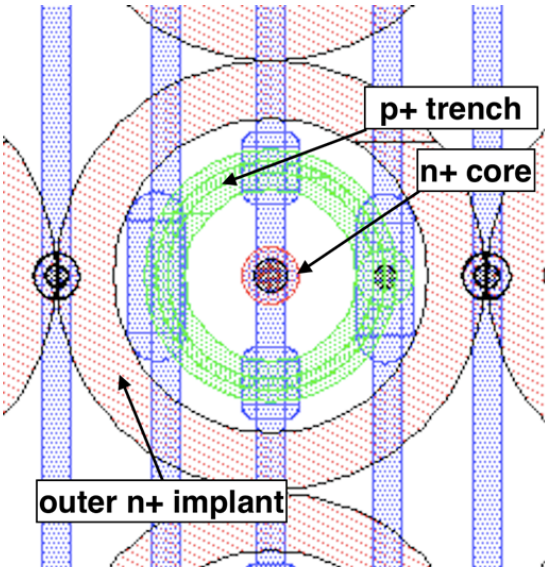

(a) Top view with guard ring present.

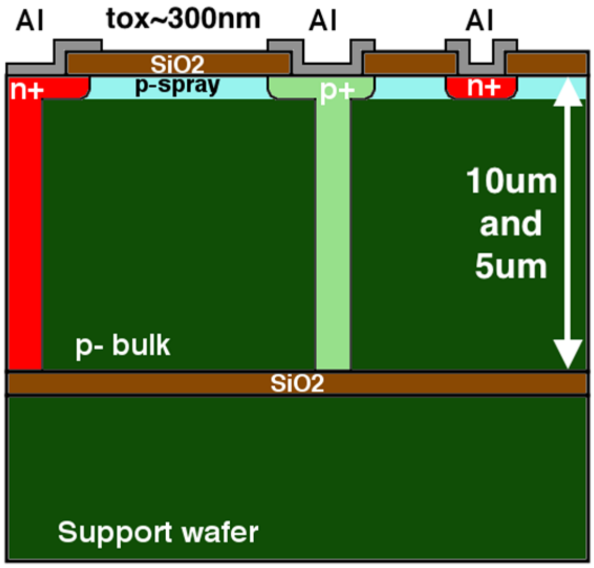

(b) Side view with 3D n+ core, 3D p+ trench, and planar n+ guard.

Figure 3.2: Layout of a 3DMiMic cell. [Povoli, 2016]

not been attempted by SINTEF yet as of the time this thesis is written. This should be done because PMMA produces secondary radiation in a very similar way to how tissue does, unlike silicon, due to the mass numbers of the atoms.

Figure 3.2b show a "3D" layout with the n+ core cylinder and the p+ trench going all the way through the bulk, and a planar n+ guard ring. There also exist designs with either or both the n+ core and p+ trench made planar. Figure 3.3 shows the smallest, "15 μm", layout of 3DMiMic from above with a size scale. The larger, "30 μm", layout has a roughly 25 % larger radius than the "15 μm" layout. The detectors with the smaller diodes have 50x50 cells, while the larger variant has 32x33 cells. Images of some of the different layouts can be found in Appendix A.

In the main layout of 3DMiMic, all the n+ cores in a line is connected together. Every second line is also connected, leaving two channels (odd/even) for readout. When present, all the outer n+ rings are connected and can be read out if desired. A full die is shown in figure 3.4, where the "+" pads are the n+ cores, the "G" pads are for the p+ trenches, the "GUARD" pads are for the cell guard rings, and the large square around the detector is a guard ring. There also exist other layouts, for example with all diodes connected together, readout in eight channels, and a larger design made to be bump bonded to a Medipix chip (see section 4.2).

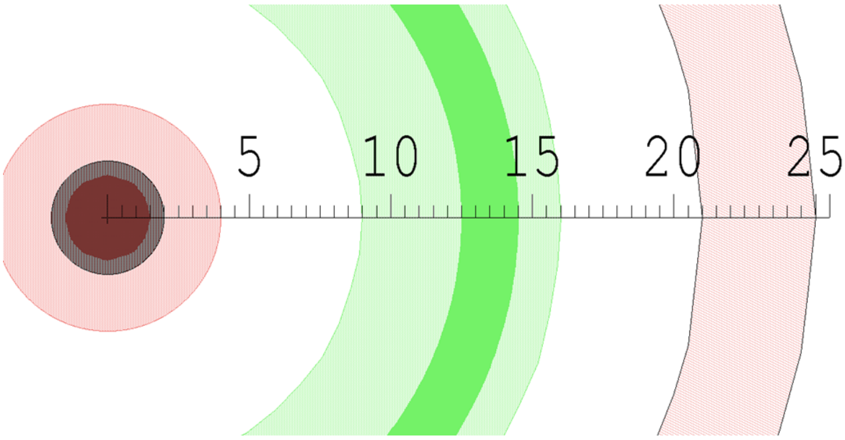

Figure 3.3: Smallest, "15 μm", layout of 3DMiMic seen from above. Distance scale is in μm. [Povoli, 2016]

Even though the odd/even readout scheme contains two channels, it does not provide any spacial information, as both channels cover the whole active area of the detector. The reason for this layout is to notice if a particle track goes through multiple adjacent cells. If both readout channels are triggered at the same time, this was not a single event, as it will look if all cells are read in a single channel.

3.3.1 3DMiMic Response to Radiation

Table XXXX from [Samnøy, 2016] show the expected signal strength in number of electrons from a Minimum Ionizing Particle (MIP) to a Carbon ion in the Bragg peak.

3.4 I-V Measurements of 3DMiMic Detectors on Wafer

I-V measurements of seven 3DMiMic wafers where performed in the cleanroom at SINTEF MiNaLab in Oslo by Øyvind Lye and Andreas Tefre Samnøy in May 2016. These seven wafers have been produced with different designs and fabrication processes. Each wafer has 104 detectors with odd/even readout, 6 detectors with single channel readout, and several other experimental layouts. The detectors had to be tested with manual needle placement, as the designs are too different to use an automatic system with a probe card. The wafer is held in place on a stand using vacuum, and the stand can be moved in the horizontal plane. The needles can be manually placed at the desired location, and the position can be fine-tuned in Cartesian space using screws. The cell n+ guard ring was not connected on the detectors where it is present. This was done because it would require a separate test setup for the detectors with the ring, which would increase the time needed for the measurement. A total of 580 detectors were measured.

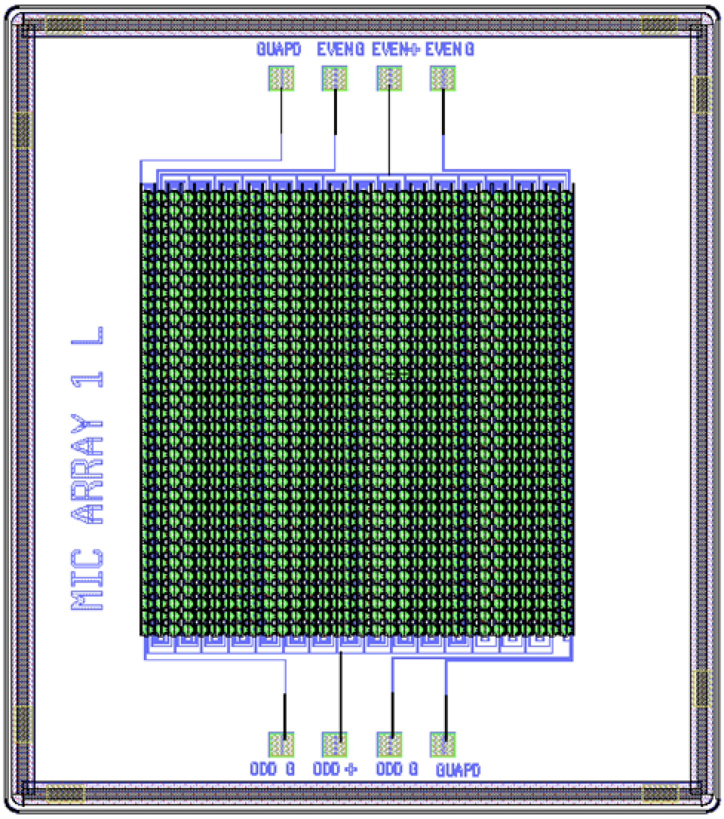

Figure 3.4: Layout of a full 3DMiMic die, showing bonding pads and the guard ring outside the active area. [Povoli, 2016]

3.5 Detector Interface PCB

A Printed Circuit Board (PCB) was designed to interface 3DMiMic to the supply and readout electronics. This is described in detail in appendix B.

3.6 Wire Bonding

Wire bonding the detectors to the PCB was supposed to be performed by SINTEF, but they had problems with the wire bonder in June 2016 which would have led to another delay. To avoid this delay, three detectors glued to PCBs were picket up at SINTEF and brought to the cleanroom at Vestfold Innovation Park for wire bonding. The wire bonder was already loaded with 17.5 μm gold wire, and this was used even though it is thinner than necessary for the 3DMiMic detectors. Each connection was done with two parallel wires to have some redundancy in case of mechanical damage to the thin wires. The three detectors are numbered: S10-15 #128 (MIC_ARRAY_3_PSTOP_L layout), S10-17 #51 (MIC_ARRAY_1 layout), and S10-17 #128 (MIC_ARRAY_3_PSTOP_L layout). See appendix A for the differences in the wafers and layouts. See appendix B for bonding schematics.

3.7 I-V Measurements of 3DMiMic Detectors on PCB

3.8 C-V Measurements of 3DMiMic Detectors

3.9 Radiation Measurements with Americium source

Chapter 4: Choice of Readout Electronics for the 3DMiMic Detector

All readout electronics that was checked during this project can be found with relevant specifications in appendix C.

4.1 Detector Readout

In different situations, the desired output from the detector readout will be different. In some cases, it is enough to simply count the radiation quanta, and in other cases one might want to read out a energy spectrum. In both cases the readout chain starts with a pre-amplifier that produces a voltage that is proportional to the radiation charge. The output from the pre-amplifier is sent to a shaping amplifier which converts the signal to a shape that is more suitable for the next component in the readout chain. This is to select the interesting pulses and convert the analog signal to a digital signal in one way or another. [Knoll, 2010, chap. 16]

4.1.1 Pre-Amplifier

For most radiation detectors, the liberated charge is too small to be processed, which is why pre-amplifiers are needed in most detector readout chains. The pre-amplifier is located close to the detector to reduce noise. A pre-amplifier can be voltage-sensitive or charge-sensitive. A voltage-sensitive pre-amplifier has an output signal proportional to the input voltage, which will be proportional to the input charge if the detector capacitance is constant. This is not the case for semiconductor detectors where the capacitance may change with the operating parameters. A charge-sensitive pre-amplifier (CSA) has a output signal that is independent of the input capacitance as long as the amplifier gain is high enough compared to a relationship between capacitances in the system. [Knoll, 2010, chap. 16]

One often important parameter to consider in a pre-amplifier is the dynamic range, which is the range of input signal amplitudes that can be reliably measured without changing the system. The lowest measurable input signal is limited by the noise in the system, mainly in the detector, detector cables, and pre-amplifier. A signal is not

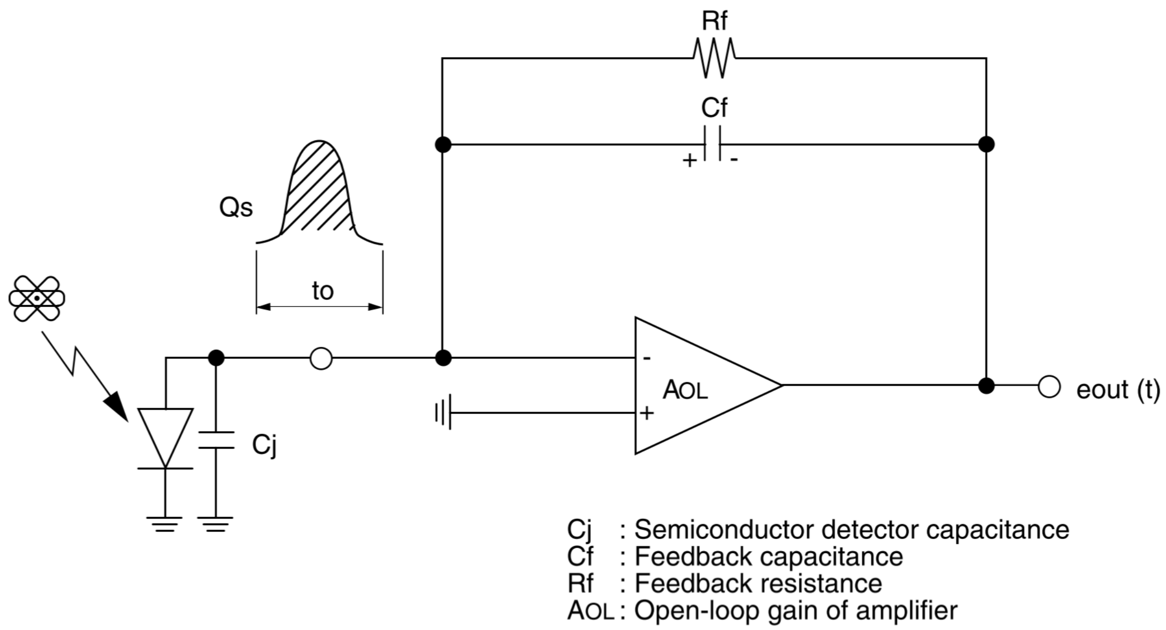

Figure 4.1: Schematic of a basic CSA. [Hamamatsu, 2001]

reliable if it is difficult to discern from the noise. The highest measurable input signal can be limited by the pre-amplifier or later stages, like the Analog-to-Digital Converter (ADC). If the pre-amplifier has a high gain, then a large input signal will require a higher output signal than the pre-amplifier can deliver. If the gain is low, then another stage in the system will likely be the bottleneck before the pre-amplifier reaches its highest output level. [Halámek et al., 2001]

It is typically convenient to use the pre-amplifier to supply bias voltage to the detector. When this is done a single cable is used both to provide voltage to the detector and to transfer the signal pulses to the readout system. [Knoll, 2010, chap. 16]

Charge-sensitive amplifier operation

Figure 4.1 shows a general CSA. When a radiation quanta strikes the detector, a pulse of charge Q_s and width t_0 is generated. This creates a rising potential on the negative input of the amplifier, which triggers a falling potential on the output of the amplifier. Because of the negative feedback, this will quickly draw the negative input close to zero, making the negative input a point of virtual ground. The feedback currents charge the feedback capacitor, and then the capacitor is slowly discharged when there is no signal on the input. This creates a voltage pulse on the output that slowly falls from a peak value that is proportional to the input charge. [Hamamatsu, 2001]

4.1.2 Shaper

The shaper, or shaping amplifier, converts the shape of the signal to a form that is suitable for measurement. The pulse height of the signal from the shaper is proportional to the input charge. It is important that the output from the shaper quickly returns to the baseline to prevent pulse overlapping that will cause measurement errors. The first stage of the shaper is a differentiator (high pass filter) which passes the steep rise of the input pulse, but quickly returns to the baseline. The differentiator decides the fall time of the pulse. The signal is then amplified to a level that is suitable for the ADC, before it is passed through the integrator (low pass filter) that filters away noise and changes the rise time of the pulse. A much used parameter to describe a shaper is the shaping time, which is related to the duration of the shaped pulse. [Knoll, 2010, chap. 16]

XXXX: More details. Noise. Ballistic defict. semi-gauss shape

4.1.3 Analog-to-Digital Conversion

The analog signal from the shaper needs to be converted to a digital signal for processing and storage. When it is desired to keep as much information as possible, an ADC is used, but these use a lot of area and power. In situations where area, power, and cost is more important than accuracy of measurements (typically when there are a lot of channels), there are some simpler methods that can be used instead. The simplest is a counter, which merely counts the number of pulses with a height above a defined threshold. The information on the radiation quanta energy is lost, but the circuit is very simple. It is also possible to have multiple counters with different thresholds, which will keep some information about the distribution of radiation quanta energies. Another much used method is the Time over Threshold (ToT) technique. A ToT circuit measures the time that the pulse is over a defined threshold, and then this measurement can be used to estimate the height of the pulse. The relationship between pulse height and ToT is only linear within a certain range, and will usually limit the dynamic range of the readout system. [Iniewski, 2010, chap. 6]

An ADC samples the analog signal amplitude at a certain interval (sampling rate) and converts each sampled value to a digital signal. The resolution, which is the number of bits in the digital signal, will limit the accuracy of the conversion. The quantisation error is introduced as each analog value needs to be converted to the closest digital value. The maximum percentage quantisation error can be seen in equation 4.1, where n is the number of digits in the binary code and 2^n is the number of digital values.

[Bentley, 2005, chap. 10]

$$e_q^{MAX} = \pm \frac{100}{2(2^n - 1)} \% \tag{4.1}$$

The dynamic range of an ADC will mainly be limited by its resolution, noise, linearity, and jitter (small timing errors). This can be summarized with effective number of bits (ENOB) to give a measure of the effective resolution, after noise and distortions. ENOB is defined as the resolution of an ideal ADC that would have the same effective resolution as the ADC in question.

4.1.4 Digital Signal Processing

4.2 Medipix and Timepix

Medipix is a family of chips developed to exploit technology from the experiments at CERN in other fields of science, mainly medical imaging. The chips made by the Medipix collaboration are; Medipix1, Medipix2, Timepix, Medipix3, Timepix3, and Dosepix. The Medipix 1-3 chips are made for photon counting and are therefore not useful for dosimetry. The Timepix chips are made to do ToT measurements, with Timepix and Timepix3 being based on Medipix2 and Medipix3 respectively. Dosepix is a currently in development chip made for photon dosimetry. They have extremely good noise properties, down to 60 e- of noise without a detector connected for Timepix3. Timepix3 and Dosepix were considered for the 3DMiMic project, but as ToT devices their dynamic range is not very large. Also, since they are made for photon detectors they cannot read the large charges released by a carbon ion in the Bragg peak.

4.3 UiO Portable Front-End Readout System

During the school year 2014-2015 two master students at UiO made a portable front-end readout system for radiation detectors [Tali, 2015] [Oltedal, 2015]. This system consists of two custom made cards and a Field-Programmable Gate Array (FPGA) evaluation board. The first card, the analog card, has three channels with pre-amplifiers while two of those channels also including shapers. The second card, the digital card, includes an ADC, comparators, and current monitors. The components of the digital card is connected to the FPGA on the SoCKit evaluation board by Arrow, which is connected to a computer through network. The system is made to detect fission fragments which produce very large signals, and therefore has a low gain. This makes the system too noisy for the low noise requirements of the 3DMiMic detector at the default gain, but this can be changed using external components.

4.4 IDEAS Amadeus Preamp-Shaper

IDE1180, or Amadeus, by Oslo-based IDEAS is an Application-Specific Integrated Circuit (ASIC) for the front-end readout of radiation detectors. It features 16 channels of CSA and shapers with adjustable shaping time. The preliminary datasheet [Maehlum et al., 2015] specifies a shaping time between 20 ns and 40 ns, negative and positive input charges up to 400 fC with lowest gain, and equivalent noise charge of 1106 e- plus 68 e- per pF load at default gain.

This chip was considered by multiple projects at IFT and a evaluation board (7045) was given to IFT so that more extensive tests could be performed. Later, a second evaluation board (7048) was also received from IDEAS. The IDE1180 characterization is described in chapter 5.

4.5 Ortec 142A Pre-Amplifier

Ortec 142A is a single channel low-noise CSA optimized for charged particle or heavy-ion detectors. It was considered for the 3DMiMic project since UiB already owns a few of these. It features a very high dynamic range, up to 55 Me-, and an equivalent noise charge between 444 e- and 944 e- for detector capacitances between 0 pF and 100 pF. The University does not have a fitting portable shaping amplifier that can be used with the 142A, and it was therefore not prioritized for this project.

4.6 Portable PCIe ADC System

The current ADC system used at UiB is a Caen V1729A digitizer sitting in a VMI crate. This features four 14 bit channels with 2 GS/s sampling rate, but is very large and heavy, making it cumbersome to bring for radiation tests. It was desirable to purchase a new ADC for the department that could be put inside a small computer using Peripheral Component Interconnect Express (PCIe) to make a portable system. Three manufacturers that produced suitable ADCs for a reasonable price were found; AlazarTech, Keysight Technologies, and SP Devices. The considered models are listed in table 4.1.

The Keysight model was interesting with a signal interleaving feature where both

Table 4.1: The analog-to-digital converters considered for purchase.

Manufacturer	**Model**	**Channels**	**Resolution** (bits)	**Sampling** (GS/s)
AlazarTech	ATS9360	2	12	1.8
Keysight	U5303A	2 (1)	12	1.6 (3.2)
SP Devices	ADQ14AC-2X	2	14	2
SP Devices	ADQ14AC-4C	4	14	1

1.6 GS/s channels could be combined into one 3.2 GS/s channel. In the end SP Devices was chosen, being the only discovered company that produces 14 bit PCIe ADCs in the GS/s range. ADQ14AC-4C was chosen since having two extra channels was considered more important than higher sampling rate for radiation tests, and the old Caen ADC can be used for projects and tests that require higher sampling rate.

4.6.1 PC for ADC

A computer to host the SP Devices ADC was needed. As this computer will be brought around to radiation tests, it was desirable to purchase as small a computer as possible to make this easier. The main requirement for the computer is that it is able to transfer data over PCIe close to the maximum data transfer rate of 3.2 GB/s specified in the ADQ14 datasheet. This puts requirements on the CPU, RAM, and motherboard. The CPU and motherboard needs to have eight available PCIe 2.0 lanes for the ADQ14. In addition, the CPU, chipset, and BIOS needs to support a PCIe payload size of 256 bytes. However, this parameter is not something CPU and motherboard manufacturers typically supply in datasheets. Also, the CPU and RAM needs to be able to handle a high load from the ADC, operating system, and software. Since most of these requirements is not something you can check in the datasheet, the safest way to assure maximum performance is to buy a high-end CPU and motherboard, and a good amount of RAM.

The main choice in computers stood between buying individual components, or purchasing a computer through a deal the IT department has with the computer manufacturers. The benefits of buying individual components would be higher certainty that the motherboard has good enough performence, and possibilities to buy a chassis of desired size. The benefits of buying a computer through the IT department is extended warranty and help setting up software. In the end, HP ProDesk 600 G2 with a micro-tower chassis was chosen. This has an Intel i7-6700 CPU, 64 GB of DDR4 RAM, a 256 GB SSD, and a 3 TB HDD.

Chapter 5: Characterization of IDE1180

IDE1180, or Amadeus, by Oslo-based IDEAS is an integrated circuit for the front-end readout of radiation detectors. It features 16 channels of CSA and shapers with adjustable shaping time. Important specifications from the preliminary datasheet can be seen in table 5.1. The gain at default settings is specified as 12.45 mV/fC. Two chips, on evaluation boards 7045-1-03 and 7048-1-04 was characterized by the author, partly together with master student Sanjeeda Sharmin and chief engineer Thomas Poulianitis. The tests have been focused on the 7045 board as it showed the best characteristics, and if nothing else is mentioned for a measurement, this it the board that was used.

Table 5.1: Specifications from the IDE1180 datasheet [Maehlum et al., 2015].

Gain [mV/fC]	24/12/6/3 at different settings
Input range [fC]	0 to $\pm$50/100/200/400
Maximum non-linearity	3 %
Equivalent Noise Charge (ENC) [e-]	1106 + 68 per pF load at default gain
Maximum input event rate	5 MHz
Maximum power consumption	32 mW

The IDE1180 can be configured to different gains, shapes, etc. by setting different inputs on the ASIC. Some of these inputs are digital, and are set to either ground or 3.3 V. The rest are set by the current into the input. This is done by configuring a potentiometer, and connecting this to 3.3 V. The connections are done by adding jumpers to 3-pin pin-headers. The middle pin is connected to either the left side, ground, or the right side, 3.3 V. This is when looking at the PCB with the input on the left and the output on the right. No jumper should be equal to a ground connection. Using "1" and "0" to specify jumper positions can easily cause confusion, because the ground pins on the pin headers are marked with a "1" (pin 1) on the PCB. Therefore, "GND" and "3V3" is used to specify jumper positions in this chapter. An X is used for no jumper. The current in the potentiometers can be checked for future reference by connecting it to ground through a 10 kΩ resistor using a GND jumper. The voltage across this resistor can be measured using a multimeter, and gives the current when divided by 10 kΩ.

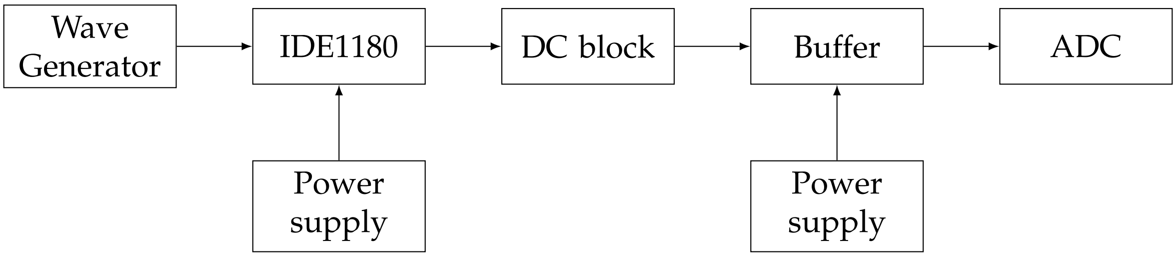

Figure 5.1: Measurement setup using the ADC.

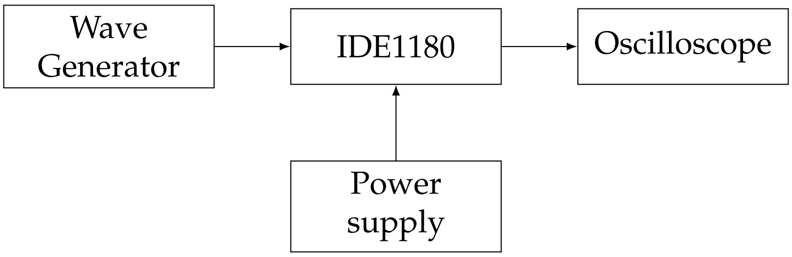

Figure 5.2: Measurement setup using an oscilloscope.

5.1 Measurement Setups

The main measurement setup used for the characterization included the Caen V1729A ADC mentioned in section 4.6. This ADC has an input impedance of 50 Ω, while the IDE1180 is configured to drive a load impedance of 1 MΩ. Therefore a in-house buffer was used between the IDE1180 and ADC. The in-house buffer cuts the signal at 750 mV (XXX double check) which makes the ADC unusable for measurements that need to cover the entire dynamic range of IDE1180. By default, the IDE1180 has an output offset voltage of 0.5 V. Since the ADC has an input range from -1 V to +1 V, a 100 nF capacitor was used to remove the offset. Some measurements used an oscilloscope instead of the ADC, which made the buffer and DC blocking capacitor unnecessary. Three different oscilloscopes have been used: Tektronix MSO 4034, Tektronix DPO 7254, and Agilent InfiniiVision MSO-X 3104A.

A wave generator was often used to simulate the pulse from a detector. This has mainly been configured to a ramp with a long rise time and a fall time as short as possible. At first, Agilent 3325OA was used, but this generator was unable to produce a quick falling edge when a long rise time was used. The Tektronix AFG3252 wave generator was later used to obtain a rise time of 1 ms. The wave generator is mainly connected to the external calibrate input, where a test capacitance of 1 pF is present in series (see figure 5.3). The input charge to the pre-amplifier is then equal to 1 pF times the peak-to-peak voltage of the test pulse from the generator.

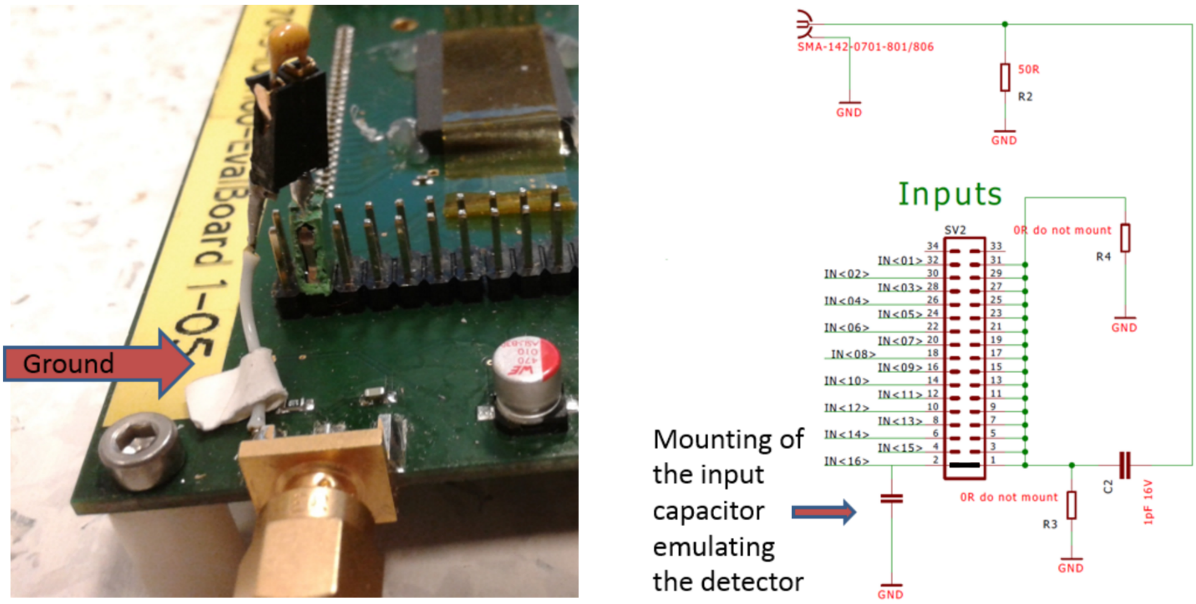

Figure 5.3: Image and schematic of capacitor mount. [Poulianitis, 2016] [Maehlum, 2015]

For many measurements it is required to vary the input load capacitance of the preamplifier, to simulate different detector capacitances. To make this possible, a mount was added that can be used to place through-hole capacitors, see figure 5.3. This connects the capacitor between the input of one channel and ground. A similar mount was made to connect an input to the output offset voltage.

The IDE1180 has been configured to six different shaping times: 40 ns (default), 100 ns, 300 ns, 500 ns, 1 μs, and 2 μs. The 100 ns and 300 ns settings have only been used to investigate the relationship between noise and shaping time. Table 5.2 shows the necessary parameters to configure the IDE1180 to these shaping times. 40 ns is the default shaping time, and therefore requires no jumpers. The voltages specify the potential that should be across the 10 $k\Omega$ resistor belonging to said signal.

Table 5.2: Configurations for different shaping times on IDE1180.

Shaping time	**PZ_ENABLE**	**PZ_BIAS_HI**	**SH_BIAS**	**VFS_BIAS**	**PZ_BIAS**
40 ns	X or GND	X or GND	X or GND	X or GND	X or GND
100 ns	3V3	X or GND	3V3, 144 mV	3V3, 132 mV	GND, 110 mV
300 ns	3V3	3V3	3V3, 308 mV	3V3, 81 mV	GND, 1790 mV
500 ns	3V3	3V3	3V3, 325 mV	3V3, 81 mV	GND, 500 mV
1 μs	3V3	3V3	3V3, 350 mV	3V3, 92 mV	GND, 268 mV
2 μs	3V3	3V3	3V3, 357 mV	3V3, 91 mV	GND, 109.5 mV

5.2 Gain vs. Input Load Capacitance

During early measurements it quickly became evident that the output voltage from the IDE1180 is reduced when the input load capacitance is increased. This drop was not understood or expected by anyone involved in the measurements, or professor Kjetil Ullaland. Tables 5.3 to 5.6 show gain measurements with different gain settings, using different setups. The oscilloscope measurements are done by placing a cursor in the middle of the noise. The ADC measurements are calculated from the mean of a gaussian fit to the amplitude measurements done by the ADC.

Table 5.3: Gain [mV/fC] vs. capacitance for different gain settings measured with oscilloscope without buffer connected.

PA_GAIN<1:0>	**0pF**	**10pF**	**56pF**	**100pF**
"GND-GND"	11.4	10.1	6.6	5.1
"GND-3V3"	7.0	6.3	4.6	3.8
"3V3-GND"	4.3	4.1	3.4	3.0
"3V3-3V3"	2.3	2.2	2.0	1.76

Table 5.4: Gain [mV/fC] vs. capacitance for different gain settings measured with oscilloscope with buffer connected.

PA_GAIN<1:0>	**0pF**	**10pF**	**56pF**	**100pF**
"GND-GND"	10.2	8.6	5.4	4.3
"GND-3V3"	6.0	5.4	4.0	3.2
"3V3-GND"	3.6	3.5	2.9	2.5
"3V3-3V3"	2.0	1.9	1.6	1.4

Table 5.5: Gain [mV/fC] vs. capacitance measured with ADC.

PA_GAIN<1:0>	**0pF**	**10pF**	**56pF**	**100pF**
"GND-GND"	10.8	9.4	5.8	4.5

As the ADC measurements takes the maximum peak signal, while the oscilloscope measurements are done with cursors in the center of the peak noise, it was expected that the table 5.5 values were slightly higher than the table 5.4 values. The values in table 5.4 are 10 to 20 % lower than those in table 5.3, showing that the in-house buffer does not perfectly pass the signal. The values in table 5.6 are 8 to 15 % lower than those in table 5.3. It should also be noted that the measured gains at 0 pF are very different from the gains of 24/12/6/3 that are noted in the datasheet [Maehlum et al., 2015].

Table 5.6: Gain [mV/fC] vs. capacitance for different gain settings measured with oscilloscope without buffer connected. Input load capacitor connected to V_{offset} instead of ground.

PA_GAIN<1:0>	**0pF**	**56pF**	**100pF**
"GND-GND"	10.2	5.8	4.44
"GND-3V3"	6.3	4.1	3.5
"3V3-GND"	3.75	2.95	2.6
"3V3-3V3"	2.05	1.75	1.5

Gain versus capacitance and gain for different gain settings was also measured on the 7048 chip. On this chip, unlike the 7045, the gain was different with no jumpers in place, and with jumpers in the left, "GND", position. It is also interesting to see that for the 7045 board, gain setting "GND-GND" gives the highest gain, while on the 7048 board "3V3-3V3" has the highest gain. XXX sjekke om pcb er lik (måle spenning på pinner)

Table 5.7: Gain [mV/fC] vs. capacitance measured with ADC on the 7048 PCB, with no jumpers in place.

PA_GAIN<1:0>	**0pF**	**10pF**	**56pF**	**56pF**	**100pF**
"X-X"	3.19	2.66	2.23	1.51	1.12

Table 5.8: Gain [mV/fC] measurements for different gain settings measured with oscilloscope on the 7048 evaluation board.

PA_GAIN<1:0>	**Gain**
"00"	5.4
"0X"	5.2
"01"	3.45
"X0"	5.3
"XX"	3.2
"X1"	2.35
"10"	2.2
"1X"	1.8
"11"	1.0

Figure 5.4 shows how the gain falls off for the different shaping times. The drop becomes less and less distinct as the shaping time is increased, and at 2 μs the gain vs. capacitance curve is fairly flat. Note that the default shaping time curve does not fit well with the data in the tables above. XXX

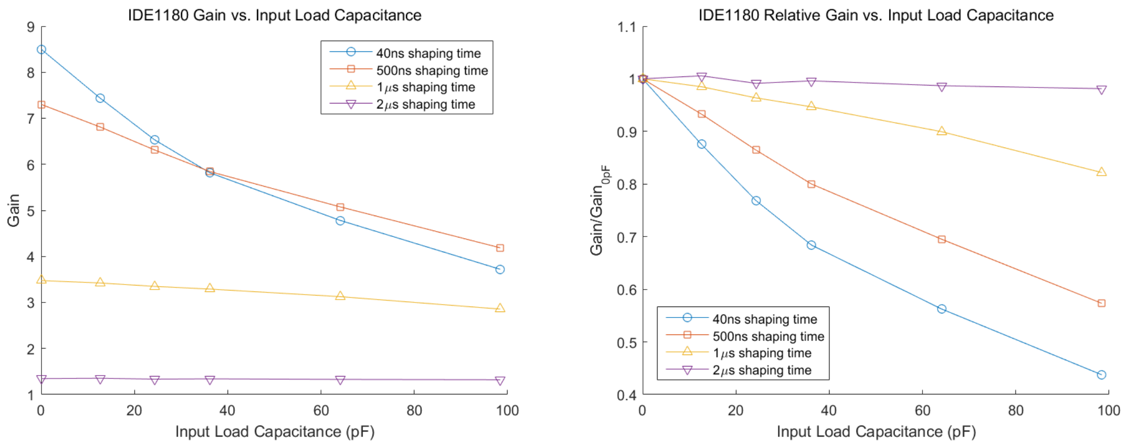

(a) Gain. (b) Relative gain.

Figure 5.4: Gain and relative gain vs. capacitance at different shaping times.

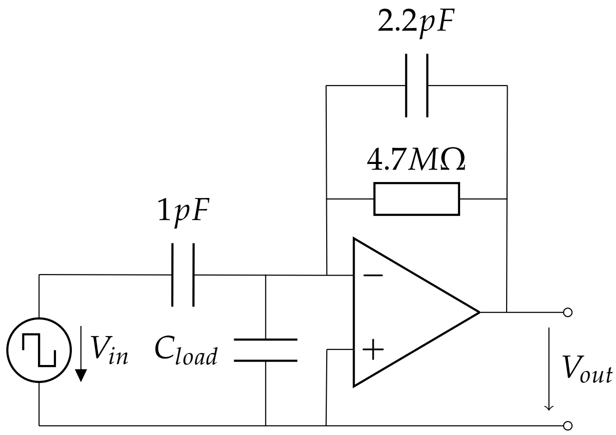

Figure 5.5: Schematic of simulated circuit.

XXX teste om forskjell på gain skyldes dc block før/etter buffer. Eller annen signalgenerator. kanskje fordi 1pf ble byttet ut (29.04)....

5.2.1 Gain vs. Capacitance Simulations

To check if the drops in gain is something that should have been expected or not, a pre-amplifier was simulated in LTspice IV. One of the pre-amplifiers from [Tali, 2015] was simulated (figure 5.5), as the specifications of the IDE1180 pre-amplifier are unavailable. This was simulated both with an ideal operational amplifier (op-amp), and with the LT1122 that was used in one of the channels in [Tali, 2015]. The input signal was a square wave of 2 ms period, 100 mV amplitude, and 10 ns edge times. Simulations were performed for C_{load} of 1 pF and 100 pF.

For the ideal op-amp, figure 5.6 shows a peak height drop of roughly 9 % and an

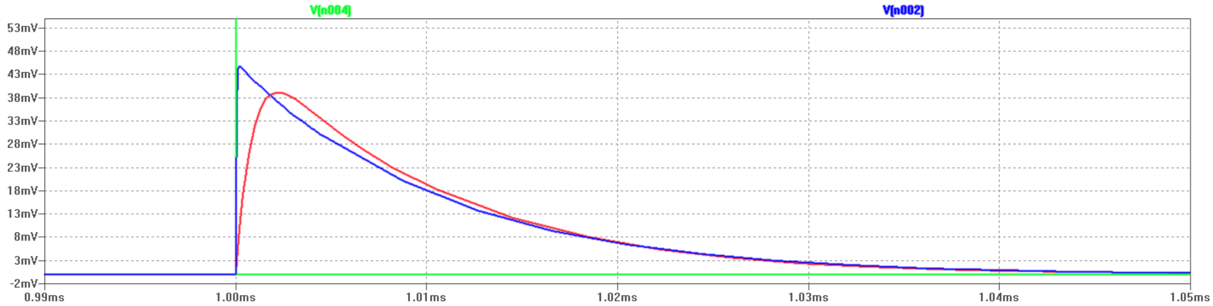

Figure 5.6: Simulation of ideal op-amp with 1 pF (blue) and 100 pF (red) load capacitance. Input pulse in green.

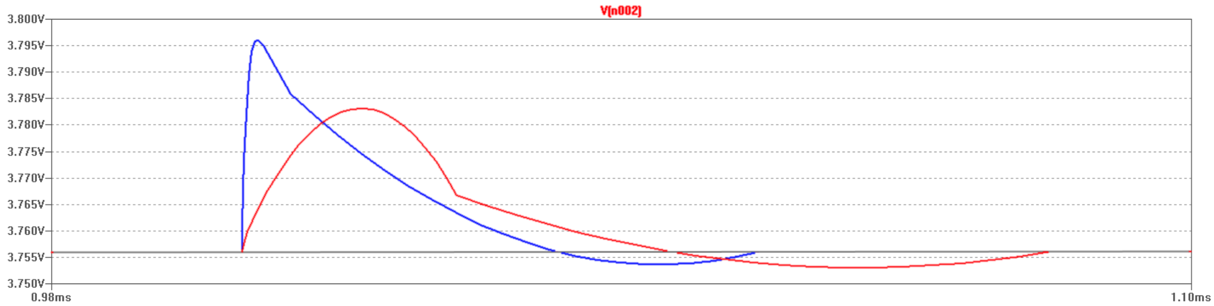

Figure 5.7: Simulation of LT1122 op-amp with 1 pF (blue) and 100 pF (red) load capacitance.

increase in pulse area of about 1 % when the load capacitance is increased from 1 pF to 100 pF. Similarly for the LT1122, figure 5.7 shows a peak height drop of about 32 % and a pulse area increase of roughly 11 %. Compared to the measured peak amplitude drops of almost 60 %, this shows that the drops should have been expected, but not in that magnitude. This has later been confirmed by figure 5.8 which shows an expected peak amplitude drop of about 10 % at 100 pF, calculated by IDEAS.

5.2.2 Ballistic defict

Ballistic defict is an error source that was investigated as a contributor to the drop in amplitude for high load capacitors. This occurs when a too short shaping time compared to the rise time of the input pulse leads to a decrease in amplitude. When the shaping time is too short, not all of the charge will have had time to be collected, and the output pulse does not reach the full amplitude. Figures 5.9 to 5.11 show measurements investigating the drop in gain by comparing the output signal from the IDE1180 when the shaper is connected and disconnected using the SH_ENABLE pin header. This is measured at default settings, using the Agilent InfiniiVision MSO-X 3104A oscilloscope. These data are based on only one curve saved from the oscilloscope, except for 100 pF with shaper disabled, where two curves were saved as the signal was very

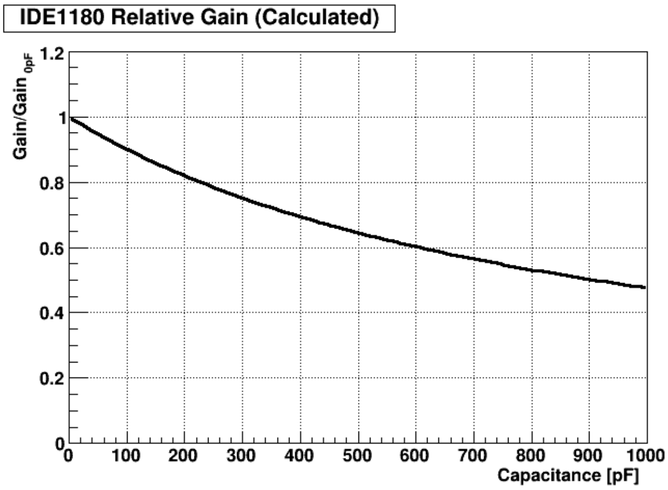

Figure 5.8: Calculated change in gain from increased input load capacitance. [Meier, 2016]

noisy. Therefore this data is not very accurate, but it is still possible to observe trends.

In figure 5.11a we see that even at 0 pF input load capacitance, the rise time of the pulse from the pre-amplifier is 60 ns, which is longer than the shaping time of 40 ns. As the capacitance is increased, the rise time is greatly increased, and we see the difference between the two curves in figure 5.9b increasing. This appears to be a ballistic defict, but as gain reduction in the shaper from the increased capacitance is only about one fifth of the total gain reduction, ballistic defict does not seem to be the main issue.

5.2.3 PCB Input Capacitance

5.3 Noise Measurements

Noise measurements on the IDE1180 have been performed with the ADC setup in figure 5.1. Three different methods have been used to measure the noise:

1. No input signal. Fit a Gaussian to the raw signal histogram.
2. With pulse on input. Fit a Gaussian to the raw signal histogram.
3. With pulse on input. Using peak detection. Fit a Gaussian to the peak histogram.

The results were expected to be somehow different on method three as it does not use the same histogram. Methods one and two looks at variations in the baseline, while method three looks at variations in the peak height. Figure 5.12 shows a comparison

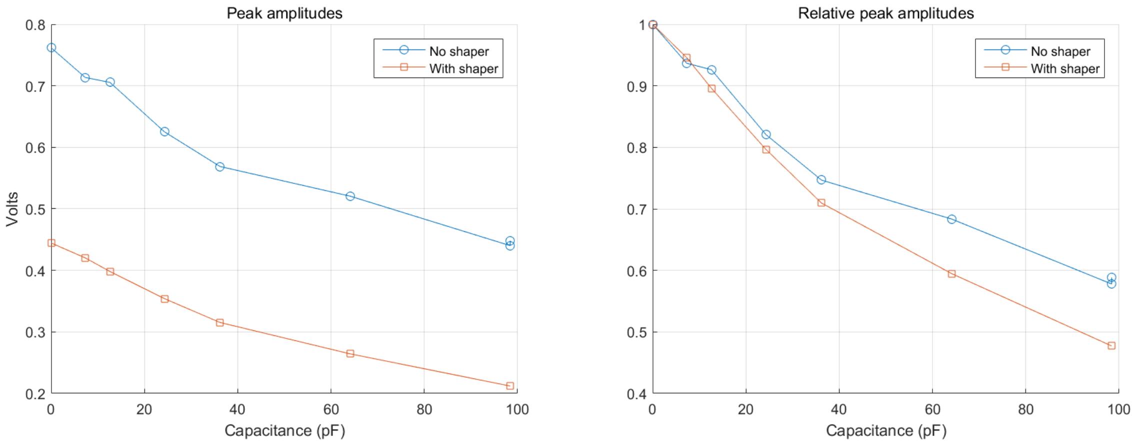

(a) Peak amplitudes. (b) Relative peak amplitudes.

Figure 5.9: Peak amplitudes and relative peak amplitudes with and without shaper connected.

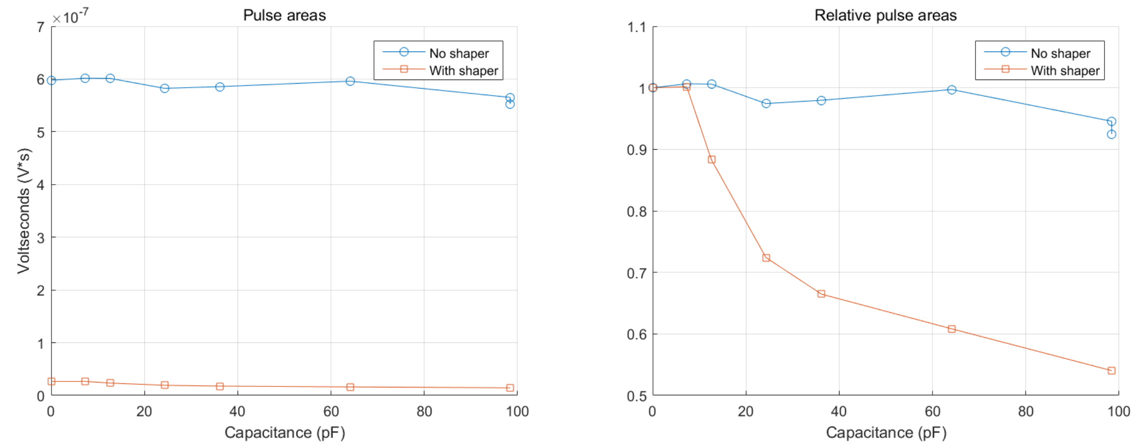

(a) Pulse areas. (b) Relative pulse areas.

Figure 5.10: Pulse areas and relative pulse areas with and without shaper connected.

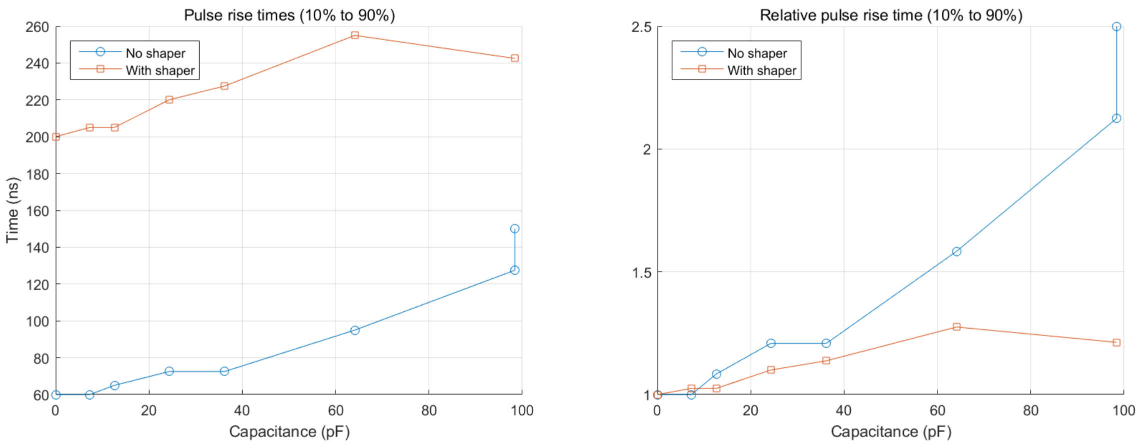

(a) Pulse rise times.

(b) Relative pulse rise times.

Figure 5.11: Pulse rise times and relative pulse rise times with and without shaper connected.

of measurement results on the same system with the three different methods. All methods show a slightly different slope. For method two, the higher noise values at high capacitance is because the histogram consists of two overlapping Gaussians.

Noise is calculated as Equivalent Noise Charge (ENC), the number of electrons needed on the input to create a signal equivalent to the measured noise, using eq. 5.1, where G is the gain, and σ (sigma) is the standard deviation of the noise histogram. The noise can also be given in full width at half maximum (FWHM) by multiplying with $2\sqrt{2 * ln2}$ (≈ 2.355).

$$ENC_{\sigma}[e-] = \frac{\sigma[mV]}{G[mV/fC] * 1.6 * 10^{-4}[fC/e-]} \tag{5.1}$$

It is unknown if the noise measurement from IDEAS, figure 5.13, is measured from the baseline variations or peak height variations, or if it is calculated as σ or FWHM. It is therefore hard to compare to this measurement.

Figure 5.14 shows a noise measurement using method 3, calculated with a gain of 12 mV/fC, as specified in the datasheet [Maehlum et al., 2015]. It is clear that the slope is extremely low, about 25 %, compared to the measurement from IDEAS in figure 5.13.

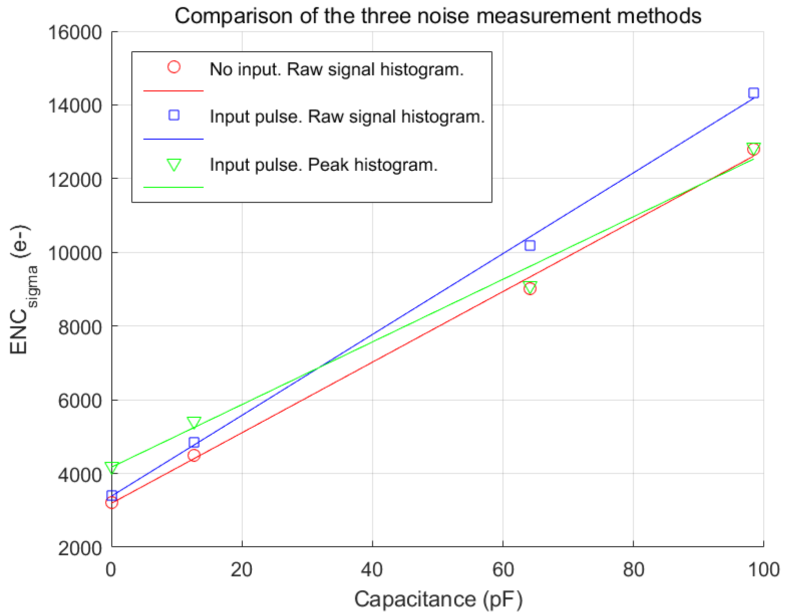

Figure 5.12: Comparison of the three noise measurement methods used.

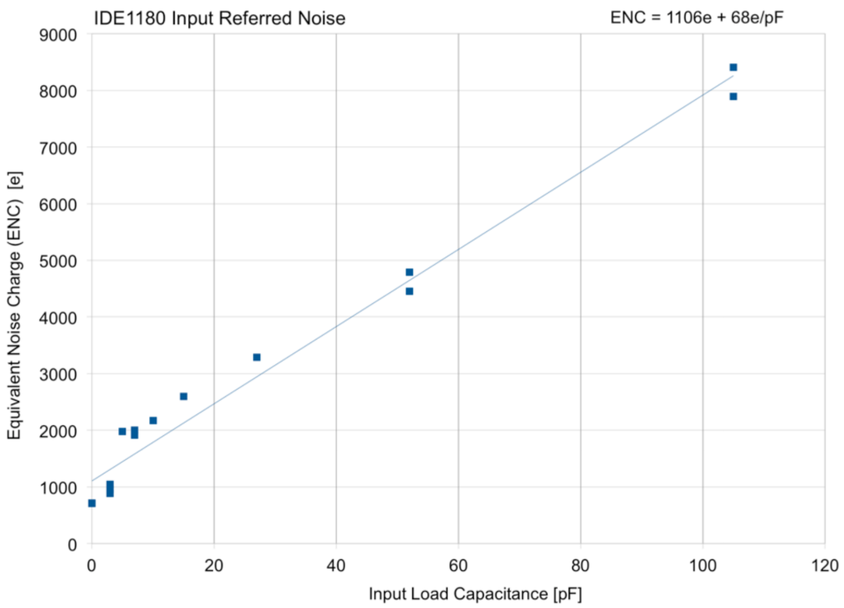

Figure 5.13: Measurement of the ENC vs. input capacitive load. [Maehlum et al., 2015]

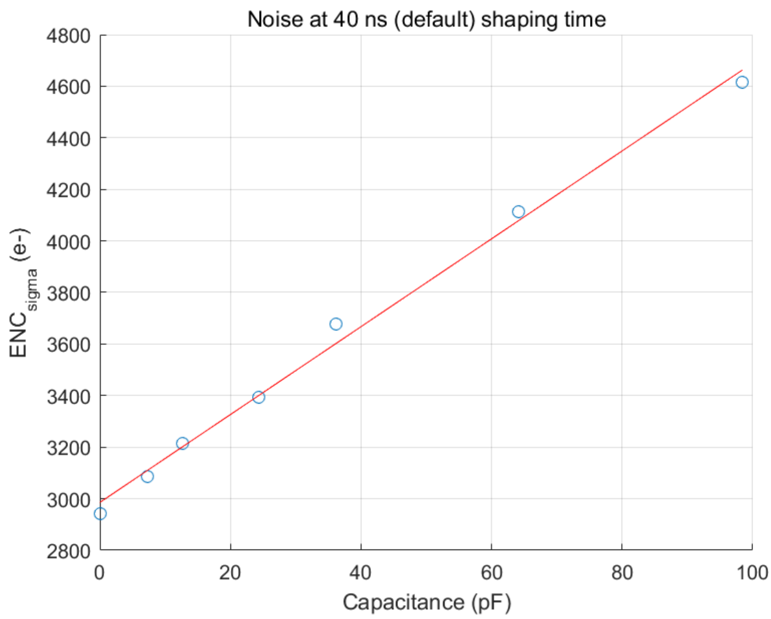

Figure 5.14: Measurement of the ENC vs. input capacitive load. Calculated with gain of 12 mV/fC.

5.3.1 Gain Compensation

As shown in equation 5.1, the gain is needed to calculate the equivalent input noise, but as discussed in section 5.2 the gain varies with input load capacitance. It is therefore necessary to change the gain for different capacitances in the noise calculation. Originally, this was done using the tables in section 5.2, but as this is not optimal in case something in the system is changed. Therefore the MATLAB script for plotting the gain was modified to also calculate the gain at each capacitance when the third method for noise measurements was used. The gain is simply calculated by taking the mean of the peak histogram and dividing by the input charge.

When gain compensation is performed, see figure 5.15, the noise curves have a slope very close to the one shown in the datasheet.

XXX figures for shaping time 0.5-2

5.3.2 Noise from Input Circuitry

Since the noise measurements in the datasheet were performed directly on the ASIC while the measurements at UiB are performed on the PCB, it is easy to assume that the differences in noise are due to the extra input circuitry on the PCB. Therefore, noise measurements were performed with six different connections on the input. This was

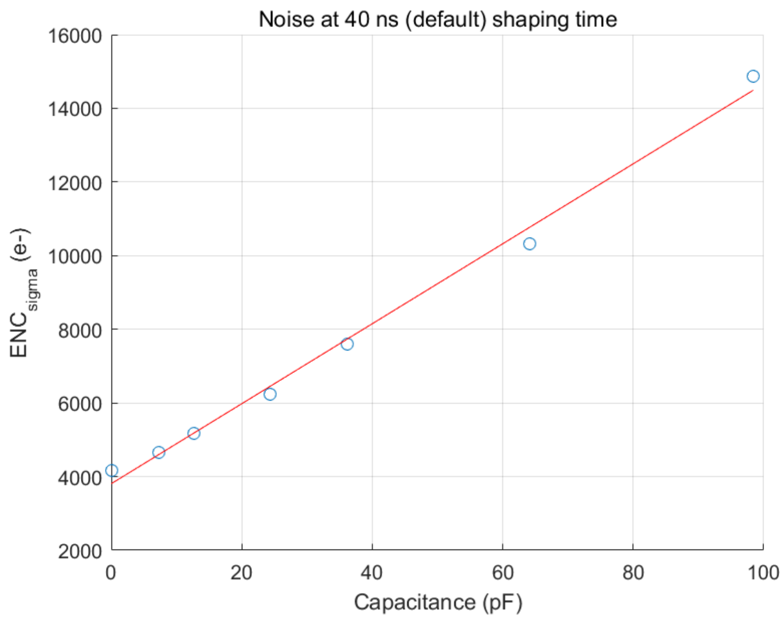

Figure 5.15: Measurement of the ENC vs. input capacitive load. Calculated with automatic gain compensation.

done with method 1 mentioned at the beginning of section 5.3 (except for measurement 6 which is using method 2), with 0 pF input load capacitance. Table 5.5 is used for gain compensation. The six connections were as following:

1. No input jumper on SV2 in figure 5.3 (SMA connector and 1pF capacitor disconnected from the ASIC).
2. Input jumper on SV2 (SMA connector and 1pF connected).
3. As 2, but aluminium foil covering input SMA.
4. Input jumper on SV2. SMA-BNC and BNC-LEMO adapters and short LEMO cable connected. Cable left floating.
5. As 4, but cable connected to wave generator. Generator powered on, but the output is turned off.
6. As 5, but with a ramp pulse from the generator output.

The main conclusion from table 5.9 is that the input circuitry has a huge impact on the noise at low capacitance. From measurements 2-5, we see that the adapters, cable, and wave generator do not contribute noticeably to the noise. We also see an increase in

Table 5.9: Noise measurements with different input circuitry connected.

Measurement #	1	2	3	4	5	6
ENC$_\sigma$ [e-]	1612	3512	3437	3462	3553	3871

noise between measurements 5 and 6, which indicates that method 2 is not a reliable form of measurement.

XXX figures for method 1 and 2, from noise docx

5.4 Gain Linearity

5.4.1 Dynamic Range

5.5 Shaping Time

The shaping time has some variations from the input load capacitance and input capacitance. The shaping times listed in table 5.2 are therefore not always accurate. Table 5.10 shows shaping time versus input load capacitance, calculated from the data that was used to create figures 5.9 to 5.11. These fluctuations appear very small and random, and could come from the noise. Figure XXX shows shaping time variations with input charge. These variations are larger, and appear more structured, with a general trend of increased shaping time with higher input charge. These data are calculated from the results of the gain linearity measurements. All the data in this section is snapshots of a single pulse, and therefore not the most accurate. If accurate measurements of the shaping time is needed, this could be done with a more complex LabVIEW program that calculates the shaping time of every pulse.

Table 5.10: Shaping time vs. input load capacitance.

Capacitance [pF]	0	7.3	12.6	24.3	36.2	64.1	90.4
Shaping time [ns]	63.0	63.5	59.5	60.0	62.0	53.5	61.0

5.6 Rise Time

plot from 40ns and x us as a b figure

table with all rise time calculations

Figure XXX shows that at 40 ns shaping time the slope increases when the amplitude increases, which makes sure that the rise time is more or less unchanged. For increased shaping time however, the slope is constant for all input charges. This leads to a greatly increased rise time for higher input charges. This unchanging slope looks very linear, which leads to the assumption that this is due to a slew rate limitations. The changes to the system performed to increase the shaping time has likely also reduced the maximum slew rate, which makes the system unable to increase the voltage fast enough.

5.7 Crosstalk

5.8 Input Sharing

5.9 Power Consumption

5.10 Pile-up

5.11 Resolution

Bibliography

ASU (2000). Arizona State University: Mechanism for the Absorption of Light. https://www.asu.edu/courses/phs208/patternsbb/PiN/rdg/mechanism/. Accessed: 14/10/2015.

Bentley, J. P. (2005). *Principles of Measurement Systems*. Prentice Hall.

Board of the Faculty of Clinical Radiology (2006). *Radiotherapy Dose-Fractionation*. Royal College of Radiologists, London.

Freeman, T. (2013). The potential of proton CT. http://medicalphysicsweb.org/cws/article/research/53211. Accessed: 15/10/2015.

Halámek, J., I. Visčor, and M. Kasal (2001). Dynamic range and acquisition system. *MEASUREMENT SCIENCE REVIEW 1*(1).

Hamamatsu (2001, 10). *Characteristics and use of Charge amplifier* (KACC9001E01 ed.). Hamamatsu Photonics.

Hysing, L. B. (2015). Geometrical uncertainties in radiotherapy. Powerpoint presentation from PHYS213 lecture October 2015 at UiB.

Iniewski, K. (2010). *Electronics for Radiation Detection*. CRC Press.

JLab. Jefferson Lab: Radiation worker training: Effects of radiation on cells. https://www.jlab.org/div_dept/train/rad_guide/effects.html. Accessed: 06/10/2015.

Khan, F. M. and J. P. Gibbons (2014). *Khan's The Physics of Radiation Therapy*. Lippincott Williams and Wilkins.

Knoll, G. F. (2010). *Radiation Detection and Measurement*. Wiley.

Lynnebakken, H. (2012). Jubler for partikkelterapi. http://www.mn.uio.no/fysikk/forskning/aktuelt/aktuelle-saker/2012/jubler-for-partikkelterapi.html. Accessed: 24/09/2015.

Maehlum, G. (2015, 11). IDE1180-EvalBoard V9 Schematic.

Maehlum, G., D. Meier, and T. Stein (2015, 11). *IDE1180 Preliminary Datasheet* (V1R3 ed.). IDEAS.

Meier, D. (2016). From email conversation.

NIH (2010). National Institutes of Health: Radiation Therapy for Cancer. http://www.cancer.gov/about-cancer/treatment/types/radiation-therapy/radiation-fact-sheet. Accessed: 09/10/2015.

Oltedal, E. J. (2015). FPGA based readout of a silicon PIN detector.

P-Cure. P-Cure Clinics. http://www.p-cure.com/index.aspx?id=4013. Accessed: 12/10/2015.

Paganetti, H. (2012). Range uncertainties in proton therapy and the role of monte carlo simulations. *Physics in Medicine and Biology 57*(11), R99.

Poulianitis, T. (2016). Project work.

Povoli, M. (2016). From email conversation.

Povoli, M. et al. (2015). Simulation and testing of thin silicon microdosimeters realized with planar technology. https://indico.cern.ch/event/351695/contributions/828320/.

Samnøy, A. T. (2016). Ph.D. work.

Schroder, D. K. (2005). *Semiconductor material and device characterization*. Wiley.

Serway, R. A. and J. W. Jewett (2014). *Physics for Scientists and Engineers with Modern Physics*. Cenage Learning.

SINTEF (2015). Si-3DMiMic - Silicon-based 3D Mini and Micro-dosimeters. https://www.sintef.no/en/projects/3dmimic/. Accessed: 24/09/2015.

Tali, M. (2015). Portable Front-End Readout System for Radiation Detection.

Young, H. D., R. A. Freedman, and L. Ford (2007). *University Physics with Modern Physics*. Addison-Wesley.

Ytre-Hauge, K. S. (2015). Radiation therapy with photons, protons and carbon ions. Powerpoint presentation from PHYS231 lecture march 2015 at UiB.

Glossary

ADC Analog-to-Digital Converter.

ASIC Application-Specific Integrated Circuit.

C-V Capacitance-Voltage.

CSA Charge-sensitive pre-amplifier.

CT Computed Tomography.

DUT Device Under Test.

ENC Equivalent Noise Charge.

ENOB Effective number of bits.

FPGA Field-Programmable Gate Array.

FWHM Full width at half maximum.

I-V Current-Voltage.

IFT Department of Physics and Technology.

LET Linear Energy Transfer.

linac Linear accelerator.

MIP Minimum Ionizing Particle.

MRI Magnetic Resonance Imaging.

op-amp Operational amplifier.

PCB Printed Circuit Board.

PCIe Peripheral Component Interconnect Express.

PET Positron Emission Tomography.

PMMA Polymethyl methacrylate.

SOBP Spread-Out Bragg Peak.

ToT Time over Threshold.

UiB University of Bergen.

UiO University of Oslo.

UOW University of Wollongong.

Appendices

Appendix A: 3DMiMic Layouts

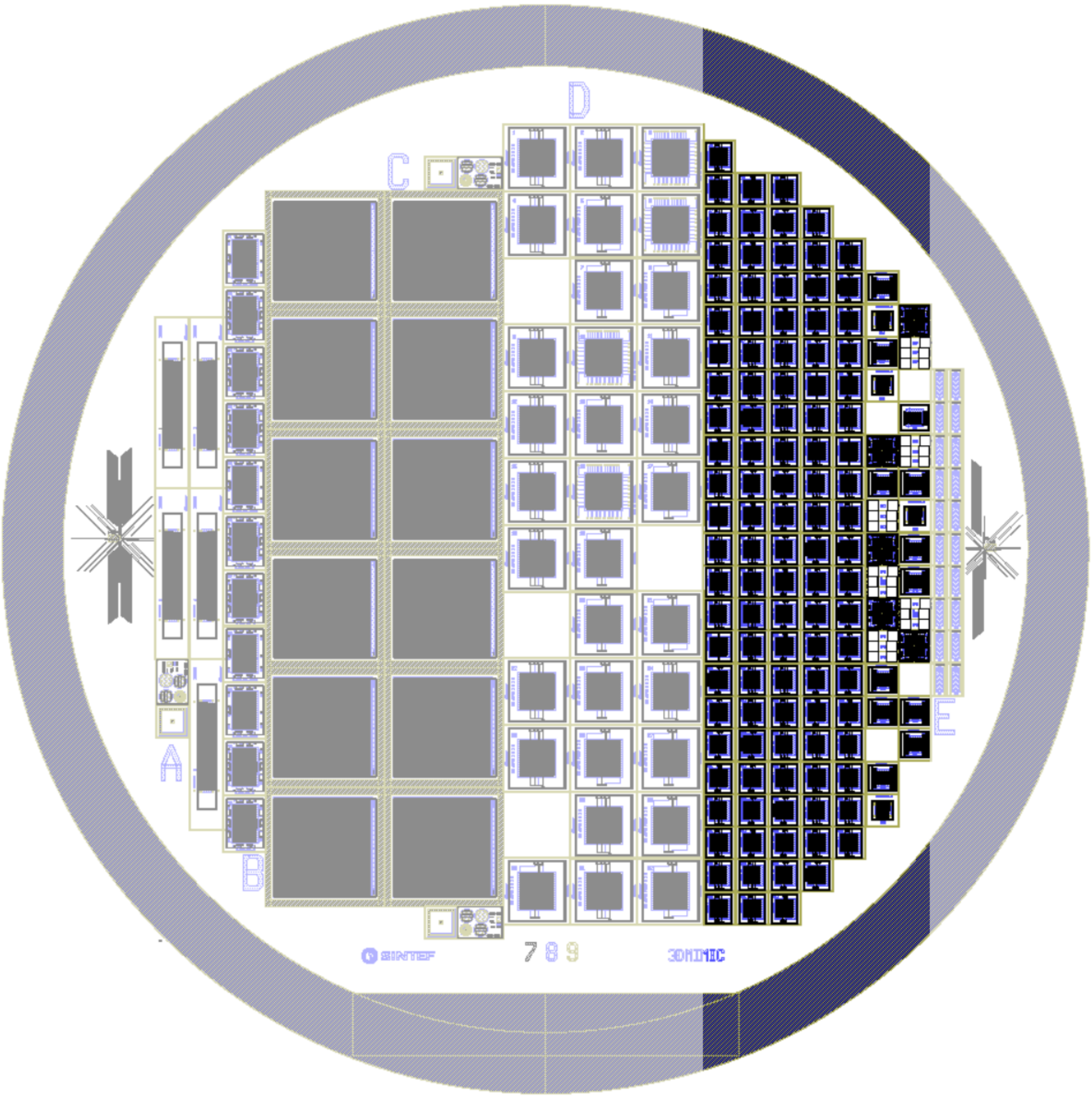

Figure A.1: 3DMiMic wafer.

Figure A.1 shows a whole 3DMiMic wafer. The highlighted area are the detectors that are relevant for this thesis. The large detectors on the left are made to be bump bonded with a Medipix chip. Figures A.3 to A.11 show some of the different layouts in the highlighted area. The detectors with "_L" in the name are of the "30 μm" size, while the others are of the "15 μm" size, see figure A.2. All figures in this appendix are from Marco Povoli at SINTEF.

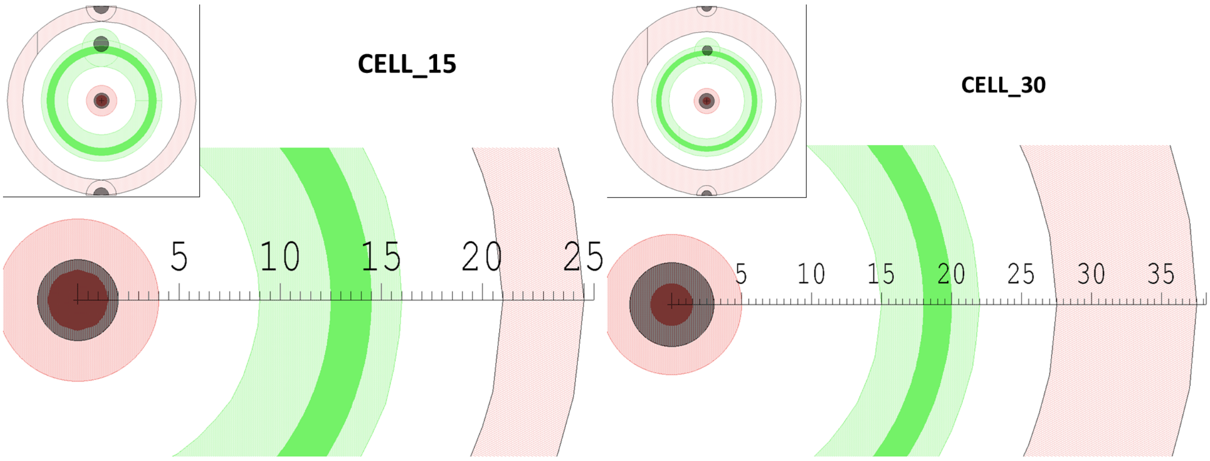

Figure A.2: 3DMiMic cell sizes. Distance scale is in μm.

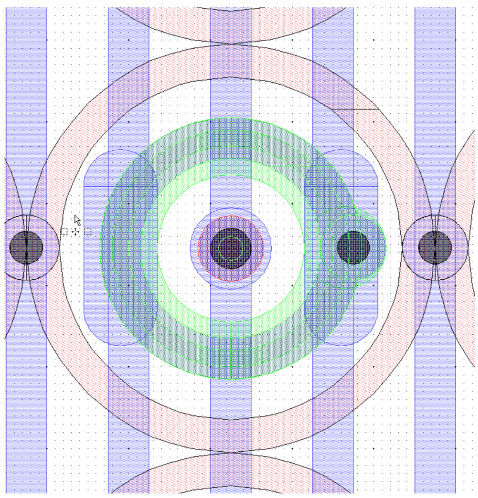

Figure A.3: MIC_ARRAY_1 layout.

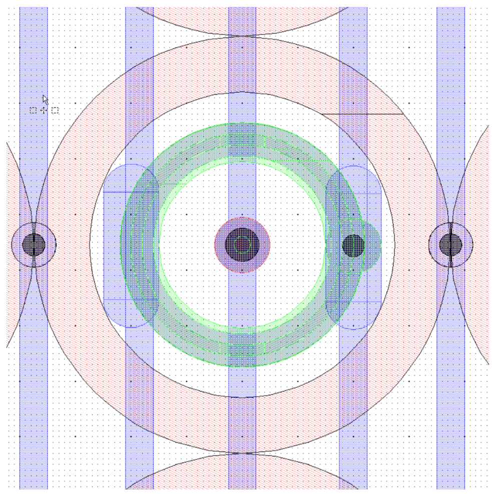

Figure A.4: MIC_ARRAY_1_L layout.

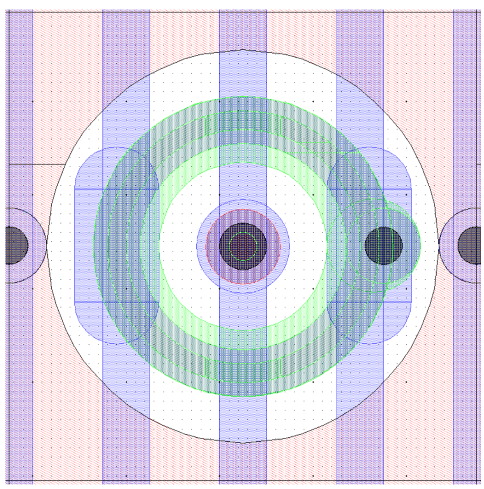

Figure A.5: MIC_ARRAY_2 layout.

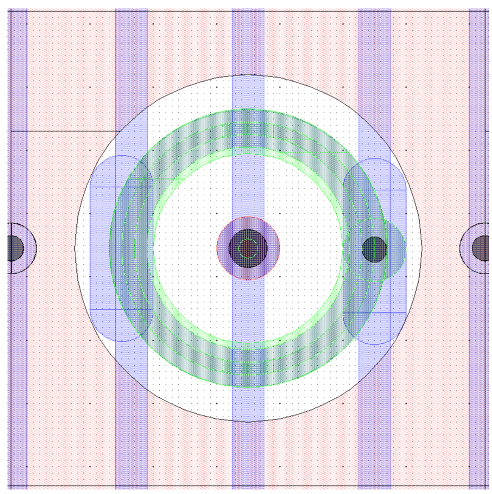

Figure A.6: MIC_ARRAY_2_L layout.

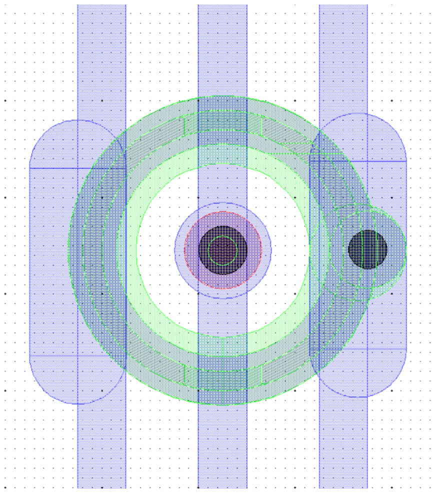

Figure A.7: MIC_ARRAY_3 layout.

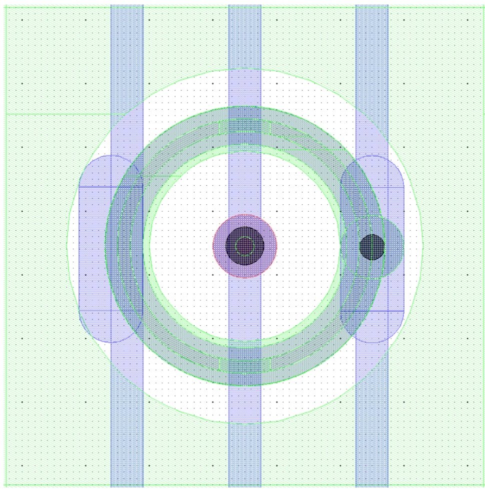

Figure A.8: MIC_ARRAY_3_L layout.

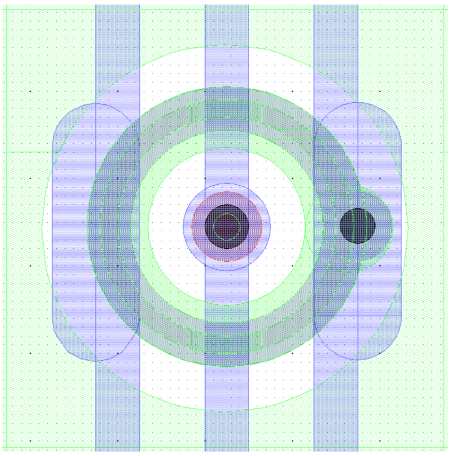

Figure A.9: MIC_ARRAY_PSTOP layout.

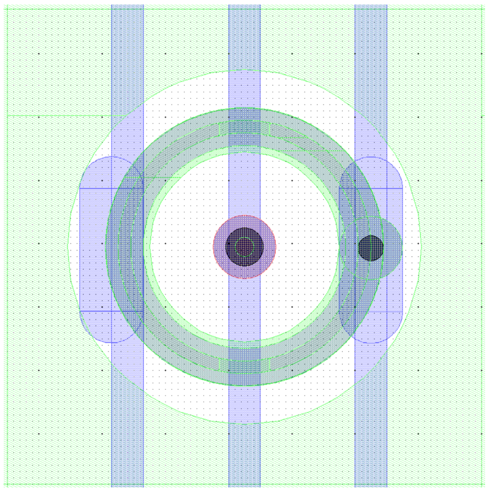

Figure A.10: MIC_ARRAY_3_PSTOP_L layout.

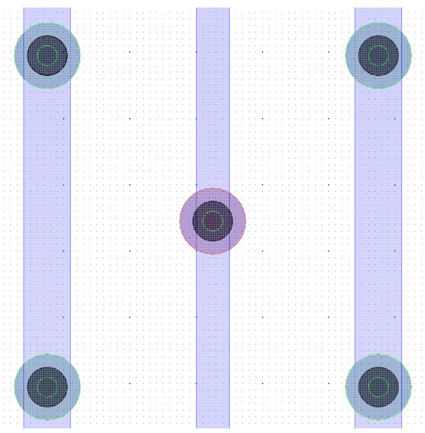

Figure A.11: MIC_3D layout. Every second column is n+ or p+ pillars.

The differences between the measured wafers are listed below [Povoli, 2016]:

S10-01 Fully planar wafer, all dopings performed with implantation.

S10-02 Same as S10-01.

S10-04 The p+ trench is NOT CLOSED and not filled with poly and is doped with gas phase, the n+ is planar and doped with implantation.

S10-11 Both p+ and n+ are etched but not filled, both dopings performed with gas phase.

S10-14 FULL 3D, both gas phase, but OLD metal (connection issues due to broken metal links).

S10-15 Both p+ and n+ etched and NOT CLOSED and not filled, p+gas phase, n+ implanted. (This wafer was tested in Japan).

S10-16 Like S10-15 but the p+ is also implanted.

S10-17 FULL 3D, complete trench and filled with poly, both doping gas phase, NEW METAL and no overetch in the process, should have better metal contacts than S10-14.

Appendix B: Detector Interface PCB

A PCB was needed to connect the detector to the outside world, as the detector pads are too small for any other connection than wire-bonding. This PCB could simply have consisted of wire-bonding pads going to connectors for cables, but it was decided to make a more multi-purpose board to make it simple to try different set-ups. The board was made so that it is possible to connect the substrate, the guard rings, and the p+ rings individually to ground or external bias. It is also possible to read out the guard rings of the cells. Each channel can also be connected to a bias filter for removal of high frequency noise. The n+ core readout channel was designed to add as little capacitance as possible. LEMO connectors were chosen to connect to the outside world as they are well shielded and much used at IFT. The exposed metal is coated with electroless nickel immersion gold (ENIG) to provide better contact for wire-bonding. One mistake was done with the PCB design in that solder mask where the detector is mounted was forgotten. This has no consequences for the 3DMiMic detector, since there is an insulating layer between the bulk and the support wafer. The solder resist can be scratched off if the PCB is to be used for a different detector. The layout of the PCB can be seen in figure B.2 and a photograph can be seen in figure B.1.

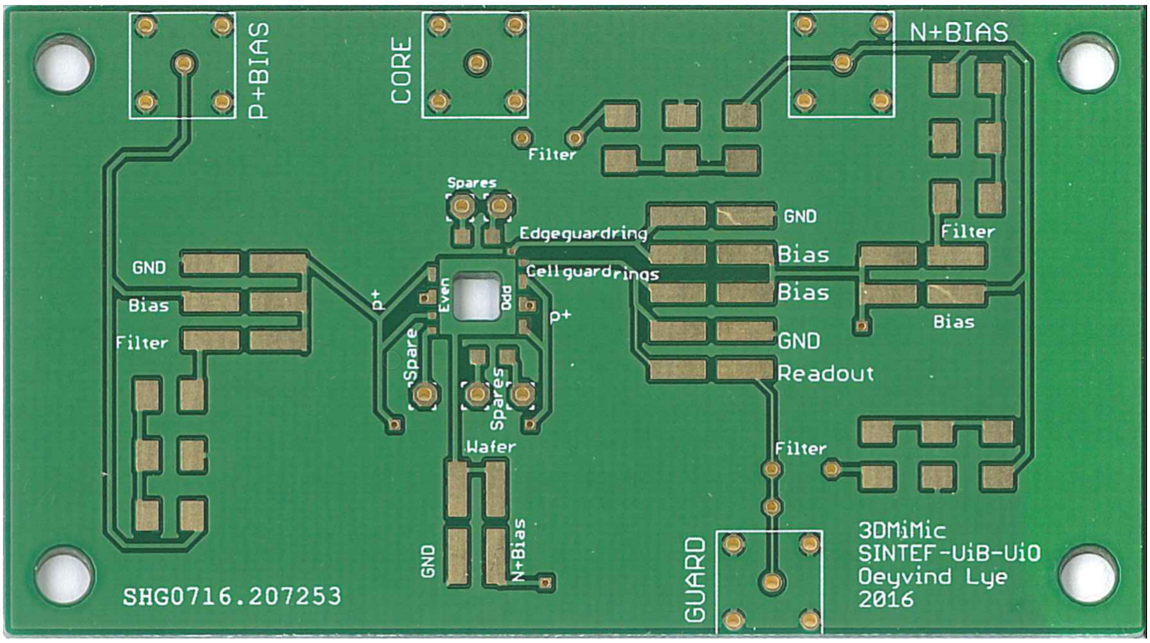

Figure B.1: Top side of PCB.

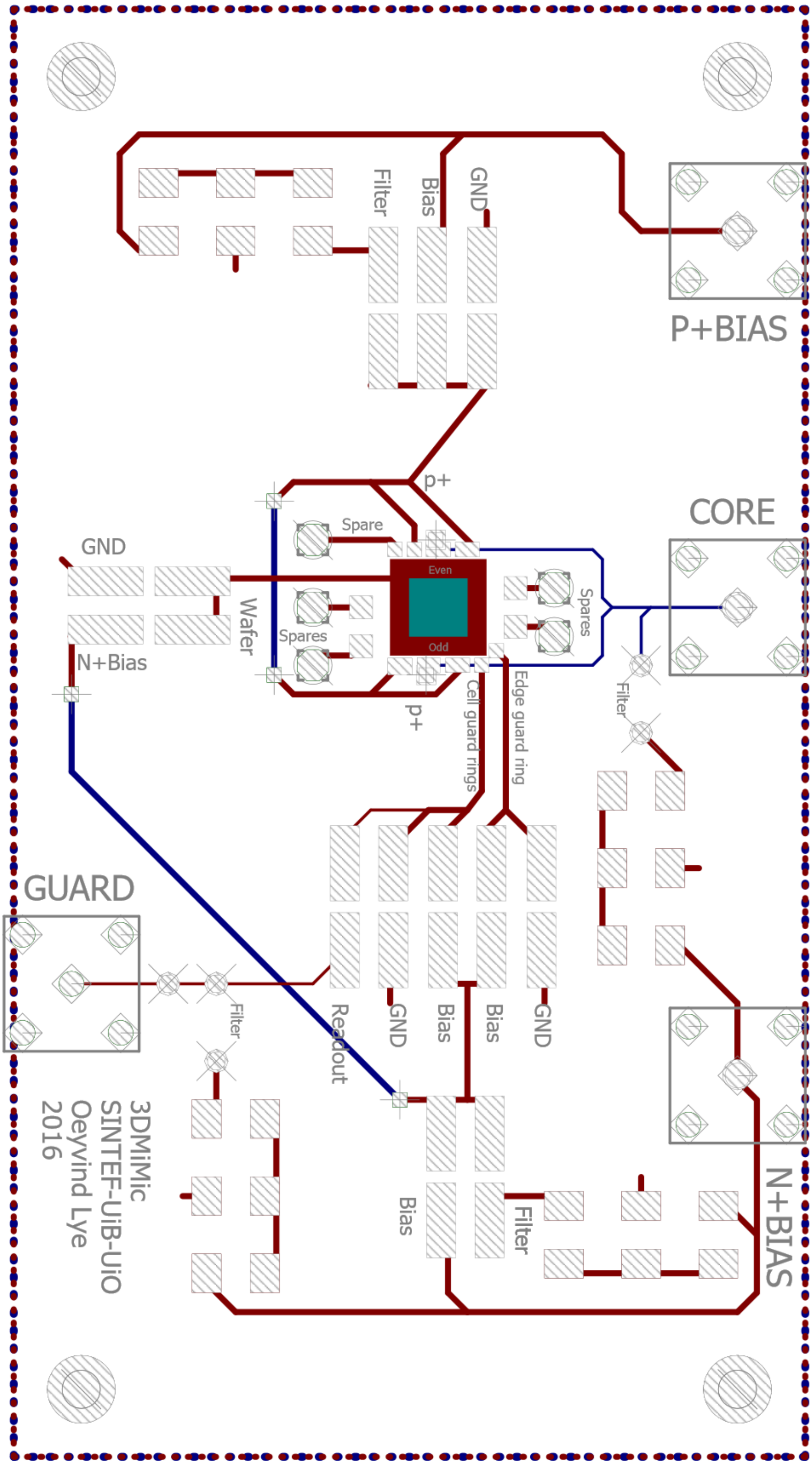

Figure B.2: PCB layout. Ground planes not shown.

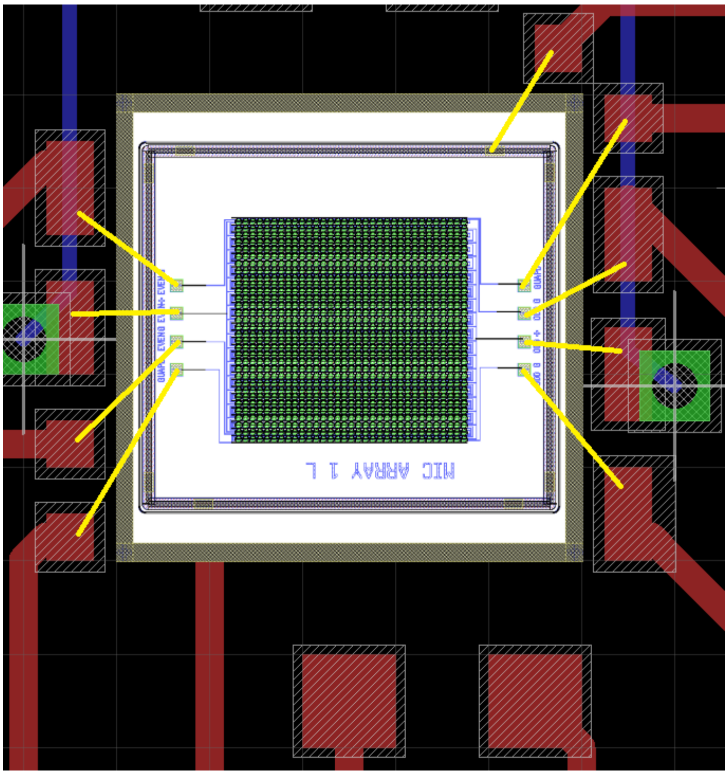

Figure B.3: Wirebonding for single channel readout on a detector with n+ guard rings.

After the design had been produced, it was again considered to read out the two sides of the detector separately, instead of in one signal. On the PCB, this can be solved by wire-bonding one of the sides to one of the spare pads and connecting this to the through-hole by the GUARD connector with a wire. To avoid extra capacitance, the wires leading to the unused surface-mounting pads can be cut with a knife. A new layout for two channel readout has been designed, and can be produced when needed.

UiB uses an X-Y table to position the detector during beam tests. This can move the detector in two dimensions with small, controlled steps. A mount was designed that can be used to connect the PCB to the X-Y table, see figure .

Picture

Figures B.3 to B.5 show how wire-bonding should be performed for different detectors and readout schemes. Figures B.6 to B.8 show where external wires (red) should be soldered, and where PCB lanes should be cut (black). Dotted line for optional wires not necessary for detector operation.

New version: two channel readout solder mask detektor detector both sides spares

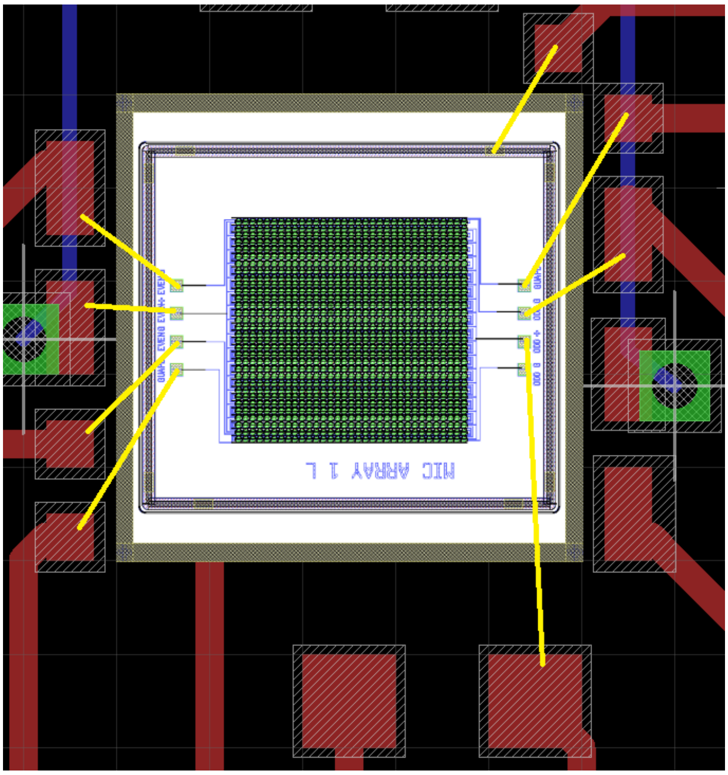

Figure B.4: Wirebonding for two channel readout on a detector with n+ guard rings.

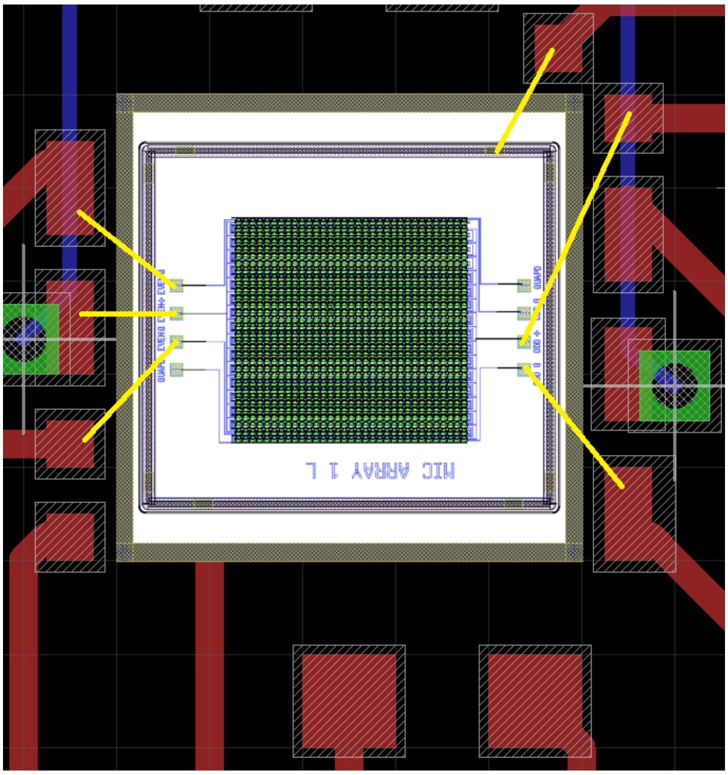

Figure B.5: Wirebonding for two channel readout on a detector without n+ guard rings.

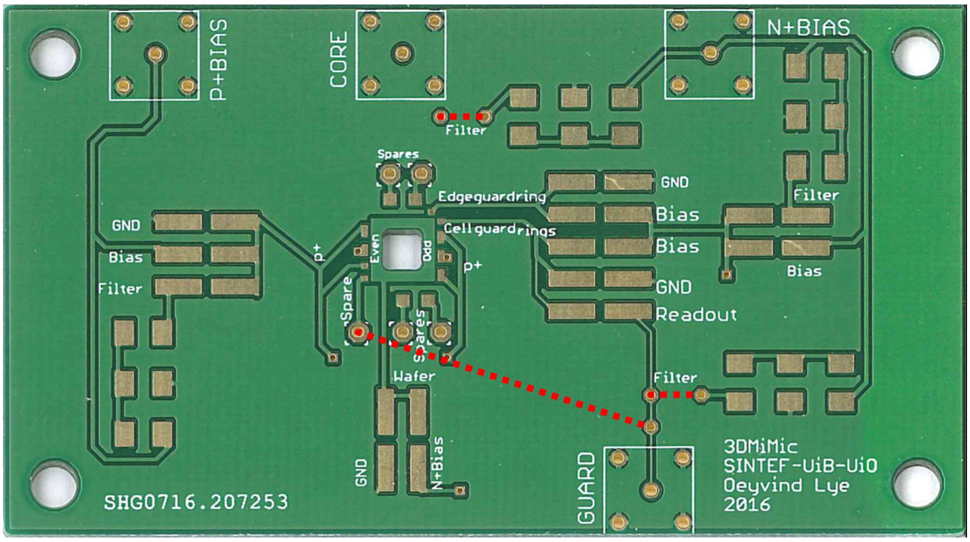

Figure B.6: Wiring for single channel readout on a detector with n+ guard rings.

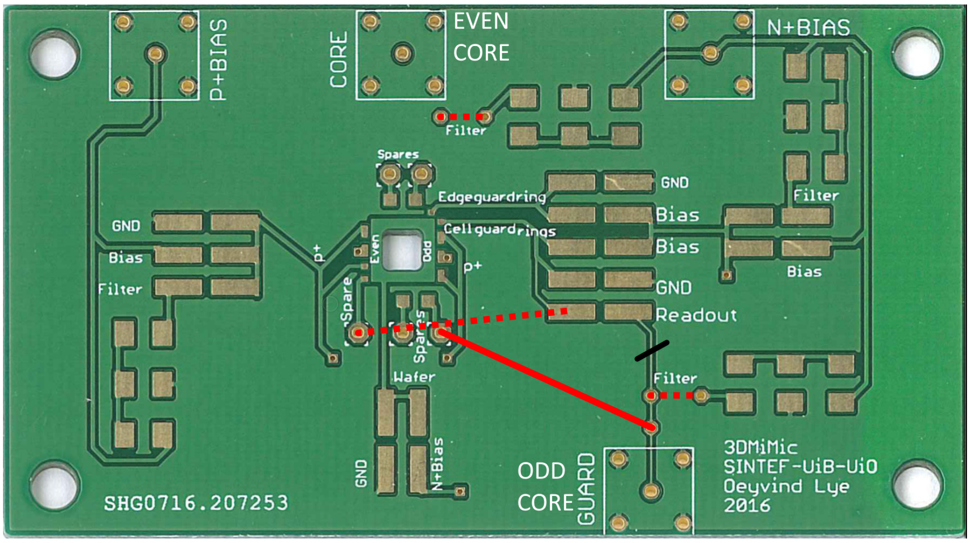

Figure B.7: Wiring for two channel readout on a detector with n+ guard rings.

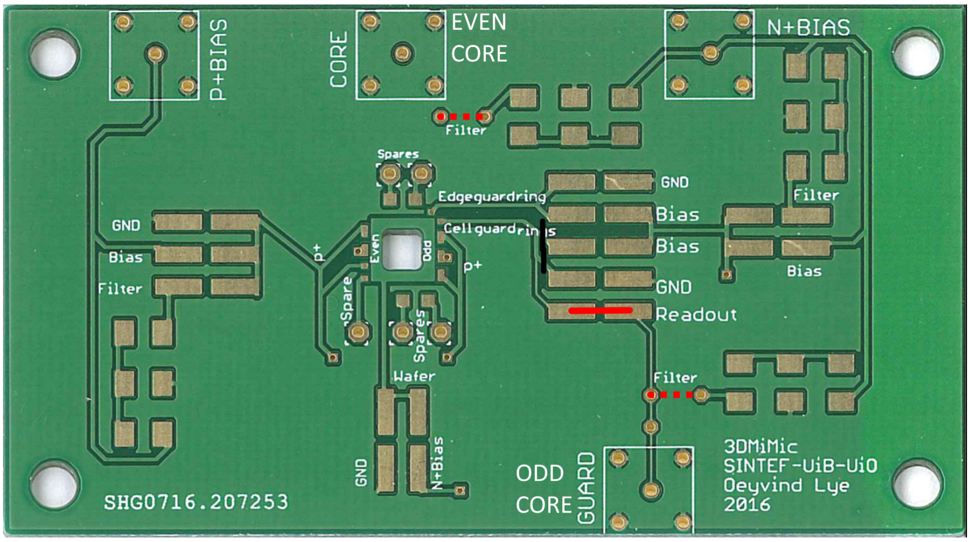

Figure B.8: Wiring for two channel readout on a detector without n+ guard rings.

closer text both sides

Appendix C: List of Readout Electronics